Calhoun
Institutional Archive of the Naval Postgraduate School

Calhoun: The NPS Institutional Archive

DSpace Repository

Theses and Dissertations | 1. Thesis and Dissertation Collection, all items

1992-06

Multispectral analysis of maritime clouds at night in the presence of atmospheric water vapor

Brooks, Christopher K.

Monterey, California. Naval Postgraduate School

http://hdl.handle.net/10945/38521

This publication is a work of the U.S. Government as defined in Title 17, United States Code, Section 101. Copyright protection is not available for this work in the United States.

Downloaded from NPS Archive: Calhoun

http://www.nps.edu/library

Calhoun is the Naval Postgraduate School's public access digital repository for research materials and institutional publications created by the NPS community. Calhoun is named for Professor of Mathematics Guy K. Calhoun, NPS's first appointed -- and published -- scholarly author.

Dudley Knox Library / Naval Postgraduate School
411 Dyer Road / 1 University Circle
Monterey, California USA 93943

AD-A256 699

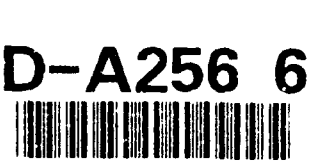

NAVAL POSTGRADUATE SCHOOL

Monterey, California

DTIC
ELECTE
NOV 0 3 1992
S
B
D

THESIS

MULTISPECTRAL ANALYSIS OF MARITIME CLOUDS
AT NIGHT IN THE PRESENCE OF
ATMOSPHERIC WATER VAPOR

by

Christopher K. Brooks
June 1992

Co-Advisor — Philip A. Durkee
Co-Advisor — Carlyle H. Wash

Approved for public release; distribution is unlimited

92-28647

251450
22 pp

REPORT DOCUMENTATION PAGE

1a. REPORT SECURITY CLASSIFICATION UNCLASSIFIED	1b. RESTRICTIVE MARKINGS
2a. SECURITY CLASSIFICATION AUTHORITY	3. DISTRIBUTION/AVAILABILITY OF REPORT Approved for public release; distribution is unlimited.
2b. DECLASSIFICATION/DOWNGRADING SCHEDULE	
4. PERFORMING ORGANIZATION REPORT NUMBER(S)	5. MONITORING ORGANIZATION REPORT NUMBER(S)
6a. NAME OF PERFORMING ORGANIZATION Naval Postgraduate School 6b. OFFICE SYMBOL (*If applicable*) 35	7a. NAME OF MONITORING ORGANIZATION Naval Postgraduate School
6c. ADDRESS (*City, State, and ZIP Code*) Monterey, CA 93943-5000	7b. ADDRESS (*City, State, and ZIP Code*) Monterey, CA 93943-5000
8a. NAME OF FUNDING/SPONSORING ORGANIZATION 8b. OFFICE SYMBOL (*If applicable*)	9. PROCUREMENT INSTRUMENT IDENTIFICATION NUMBER
8c. ADDRESS (*City, State, and ZIP Code*)	10. SOURCE OF FUNDING NUMBERS Program Element No. / Project No. / Task No. / Work Unit Accession Number

11. TITLE (*Include Security Classification*)
MULTISPECTRAL ANALYSIS OF MARITIME CLOUDS AT NIGHT IN THE PRESENCE OF ATMOSPHERIC WATER VAPOR

12. PERSONAL AUTHOR(S) Christopher K. Brooks

13a. TYPE OF REPORT	13b. TIME COVERED	14. DATE OF REPORT (*year, month, day*)	15. PAGE COUNT
Master's Thesis	From To	June 1992	82

16. SUPPLEMENTARY NOTATION
The views expressed in this thesis are those of the author and do not reflect the official policy or position of the Department of Defense or the U.S. Government.

17. COSATI CODES			18. SUBJECT TERMS (*continue on reverse if necessary and identify by block number*)
FIELD	GROUP	SUBGROUP	Spectral difference, brightness temperature, thresholds, image masking, subscenes, cloud classification

19. ABSTRACT (*continue on reverse if necessary and identify by block number*)

Multispectral analysis methods are exercised using AVHRR channels 3, 4, and 5 to improve upon single-wavelength thermal imagery at night. An algorithm was developed yielding cloud location and water vapor distribution from channel 3-4 and 4-5 differences, respectively. Water vapor effects on pixel registration for cloud were examined using two candidate subscenes, one cloudy and dry, the other, cloudy and moist. A positive water vapor/cloud-free correlation was found using statistical techniques on the candidate subscene scatter plots. TOVS water vapor channels verified the analyzed water vapor pattern in the 4-5 difference image. V-shaped cloud/clear thresholds were applied to various subscene scatter plots to account for the positive correlation of water vapor-to-cloud registration. Results showed that in regions of higher water vapor concentrations, pixels nearest cloud boundaries were likeliest to be misclassified as clear. Images containing significant water vapor gradients and cloud variations required threshold refinement for best results.

20. DISTRIBUTION/AVAILABILITY OF ABSTRACT	21. ABSTRACT SECURITY CLASSIFICATION	
☒ UNCLASSIFIED/UNLIMITED ☐ SAME AS REPORT ☐ DTIC USERS	Unclassified	
22a. NAME OF RESPONSIBLE INDIVIDUAL Carlyle H. Wash	22b. TELEPHONE (*Include Area code*) (408) 646-2295	22c. OFFICE SYMBOL MR (Wx)

Approved for public release; distribution is unlimited.

Multispectral Analysis of Maritime Clouds at Night
In the Presence of Atmospheric Water Vapor

by

Christopher K. Brooks
Captain, United States Air Force
B.A., The Ohio State University, 1983

Submitted in partial fulfillment
of the requirements for the degree of

MASTER OF SCIENCE IN METEOROLOGY

from the

NAVAL POSTGRADUATE SCHOOL
June 1992

Author: [redacted]
Christopher K. Brooks

Approved by: [redacted]
Philip A. Durkee, Co-Advisor

[redacted]
Carlyle H. Wash, Co-Advisor

[redacted]
for Robert L. Haney, Chairman
Department of Meterology

ABSTRACT

Multispectral analysis methods are exercised using AVHRR channels 3, 4, and 5 to improve upon single-wavelength thermal imagery at night. An algorithm was developed yielding cloud location and water vapor distribution from channel 3-4 and 4-5 differences, respectively. Water vapor effects on pixel registration for cloud were examined using two candidate subscenes, one cloudy and dry, the other, cloudy and moist. A positive water vapor/cloud-free correlation was found using statistical techniques on the candidate subscene scatter plots. TOVS water vapor channels verified the analyzed water vapor pattern in the 4 - 5 difference image. V-shaped cloud/clear thresholds were applied to various subscene scatter plots to account for the positive correlation of water vapor-to-cloud registration. Results showed that in regions of higher water vapor concentrations, pixels nearest cloud boundaries were likeliest to be misclassified as clear. Images containing significant water vapor gradients and cloud variations required threshold refinement for best results.

Accession For
NTIS GRA&I ☑
DTIC TAB ☐
Unannounced ☐
Justification
By
Distribution/
Availability Codes
Dist | Avail and/or Special
A-1

DTIC QUALITY INSPECTED 1

TABLE OF CONTENTS

I. INTRODUCTION 1

II. BACKGROUND 4

A. SPECTRAL VARIATION TECHNIQUES 4

B. SENSOR AND WAVELENGTH SELECTION 6

C. MULTISPECTRAL ANALYSIS WITH AVHRR CHANNELS 3, 4, AND 5 9

III. DATA AND METHODOLOGY 18

A. DATA 18

1. Case 1: 3 July 1987 19

2. Case 2: 18 July 1987 20

B. METHOD 23

IV. RESULTS 25

A. IMAGERY ANALYSIS TO REVEAL CLOUDS AND WATER VAPOR 25

1. Analysis of T_{3-4} Imagery For Clouds 25

2. Imagery Analysis For $H_2O_{(v)}$ Distribution . 29

a. T_{4-5} Imagery for Case 1 29

b. TOVS for Case 1 31

c. T_{4-5} and TOVS Imagery for Case 2 . . . 36

B. INITIAL ANALYSIS OF CASE 1 SUBSCENES 1 AND 2 . 36
C. THRESHOLD SELECTION AND ADJUSTMENT 41
1. Cloud Thresholds Using Only T_{3-4} Data . . . 41
2. Addition of T_{4-5} Thresholds 48
3. Applying $H_2O_{(v)}$ Correlation Thresholds . . 51
a. Analysis of the T_{3-4}/T_{4-5} Correlation . 51
b. Threshold Refinement in Subscenes 1 and 2 53
c. Application of Thresholds to Other Subscenes 60

V. CONCLUSIONS 69
REFERENCES 71
INITIAL DISTRIBUTION LIST 73

LIST OF FIGURES

Fig. 1. Transmittance spectrum of Earth's atmosphere. 5

Fig. 2. Infrared transmittance of water vapor 8

Fig. 3. HIRS $H_2O_{(v)}$ channel weighting functions . . . 10

Fig. 4. Relative T_B for clear/dry situation 12

Fig. 5. Relative T_B for cloudy/dry situation. 13

Fig. 6. Relative T_B for clear/moist situation 16

Fig. 7. Relative T_B for cloudy/moist situation 17

Fig. 8. Case 1 overview (channel 4) with subscenes . . 21

Fig. 9. Case 2 overview with subscenes. 22

Fig. 10. T_{3-4} image of case 1 with subscenes. 27

Fig. 11. T_{3-4} image of case 2 with subscenes. 28

Fig. 12. T_{4-5} image for case 1 with subscenes. . . . 30

Fig. 13. TOVS channel 11 $H_2O_{(v)}$ overview for case 1. . 32

Fig. 14. TOVS channel 10 $H_2O_{(v)}$ overview for case 1. . 34

Fig. 15. TOVS channel 12 $H_2O_{(v)}$ overview for case 1. . 35

Fig. 16. Case 2 T_{4-5} overview. 37

Fig. 17. T_{3-4}/T_{4-5} scatter plot for subscene 1 39

Fig. 18. T_{3-4}/T_{4-5} scatter plot for subscene 2 40

Fig. 19. Subscene 1 mask: T_{3-4}= -1; no T_{4-5} threshold 43

Fig. 20. Subscene 1 channel 4 color enhancement . . . 44

Fig. 21. Subscene 2 mask: T_{3-4}= 0; no T_{4-5} threshold . 46

Fig. 22. Color enhanced channel 4 image of subscene 2 47

Fig. 23. Mask of subscene 1: T_{3-4} = -1; T_{4-5} = 0 . . . 50

Fig. 24. Threshold slope derived through centroids . . 52

Fig. 25. Case 1 subscene 1 scatter reclassification . 54

Fig. 26. Case 1 subscene 2 scatter reclassification . 55

Fig. 27. Subscene 1 mask: T_{4-5}/T_{3-4} = -1.8/+.27 . . . 57

Fig. 28. Mask of subscene 2: T_{4-5}/T_{3-4} = +0.5/-0.8 . . 59

Fig. 29. Subscene 3 mask: T_{4-5}/T_{3-4} = +.27/-1.8 . . . 61

Fig. 30. Case 1 subscene 3 color enhancements 63

Fig. 31. Case 2 subscene 1 mask: T_{4-5}/T_{3-4} = 0.5/-0.8 65

Fig. 32. Case 2 subscene 1 color enhancement 66

Fig. 33. Modified mask for case 2 subscene 1 67

ACKNOWLEDGMENTS

To the Ultimate Source of Inspiration:

I humbly acknowledge my gratitude for my professors and advisors here at the Naval Postgraduate School, as well as for my colleagues and friends in the U.S. Navy;

For Professor Philip A. Durkee, whose vision and inspiration stimulated my interest in this project, and Professor Carlyle H. Wash, whose insight, patience, and encouragement enabled me to finish this thesis, I give special thanks;

I also acknowledge the tireless efforts of Mr. Craig E. Motell and Mr. Kurt Nielsen to instruct me on usage of the VAX system, and whose labors to update software programs for my imagery analysis were legend.

This work is dedicated to Shyrlene Stewart Brooks, my best friend and dear wife, whose radiance of love and concern at all wavelengths, day or night, produced an environment suitable for the completion of this thesis.

I. INTRODUCTION

Instruments aboard today's environmental satellites collect radiometric data at numerous wavelength channels over the electromagnetic (EM) spectrum. Users of satellite imagery readily recognize the cloud and weather patterns from these data.

Civilian and military satellite meteorologists often need to know the location and types of clouds. From a long-term or climatological perspective, accurate assessment of cloud amounts may impact current mean precipitation estimates, data bases for numerical forecasting models, and the Earth's radiation budget. On smaller time and space scales, forecasters depend on timely awareness of weather and cloud patterns. Military fleet and aviation operations, commercial merchant marine and airline industries, and the general public all require satellite imagery to enhance weather forecasting accuracy. Additionally, many of the most highly technical military weapons systems owe their successful deployment and accuracy to a correct interpretation of weather conditions, where clouds play important roles.

Single-wavelength imagery may not clearly display all clouds within the satellite's field of view (FOV), however. For a cloud to appear in imagery, radiant energy emitted from the cloud at a particular wavelength must differ sufficiently

in intensity from the background surface energy emitted. Otherwise, no contrast will exist between the cloud and background, and the cloud will not appear in the satellite image. Other factors can limit or enhance the emittance contrast between cloud and land or sea surfaces: presence or absence of sunlight, temperatures of earth and cloud surfaces, cloud thickness, and presence of emitters or absorbers in the atmosphere between cloud and satellite. In some instances, clouds may remain undetected in an image due to certain combinations of these parameters.

Gases and clouds in the atmosphere emit radiant energy in amounts that can vary greatly with wavelength over the terrestrial EM spectrum. Researchers have used these variations to create images from two or more wavelength channels, providing an effective process for revealing atmospheric features not otherwise discernible (Crosiar et al. 1989; d'Entremont 1986; Dykes 1991; Eyre et al. 1984; Hunt 1973; Olesen and Grassl 1988; Saunders and Kriebel 1988). Several studies have applied this multispectral variation method to reveal or enhance the presence of low-level stratiform clouds even when these features did not appear in imagery sensed at one wavelength alone.

The presence of water vapor in large amounts above the low clouds, however, may mitigate these encouraging research results. Water vapor is an effective absorber/emitter of energy at some of the infrared (IR) wavelengths most favored

for cloud imaging. When found in sufficient amounts between the cloud top and the satellite sensor, water vapor will absorb and emit enough radiation to significantly alter the satellite-measured radiance and resulting cloud signature. Presence of water vapor can thus diminish the effectiveness of using two channels to detect "hidden" low clouds and can again render the cloud as indistinguishable from the sea or land surface below.

The objective of this project is to use purely multispectral analysis techniques to verify the location of low clouds in a maritime environment when visible wavelength imagery is not available for verification, and where significant quantities of atmospheric water vapor may obscure imaging of cloud features below. Chapter II contains radiometric observation of clouds and water vapor and its application to this thesis. Chapter III describes the data sources used in this study and the methods used to qualify the presence of water vapor in the atmosphere and to apply that knowledge to verify the location of low-level clouds. Results are presented in Chapter IV with discussion of the cases examined, and Chapter V contains conclusions and recommended courses of action following the completion of this work.

II. BACKGROUND

A. SPECTRAL VARIATION TECHNIQUES

A satellite radiometer simultaneously measures emitted radiant energy at several different wavelength bands within the visible (VIS), IR, or microwave (MW) portions of the EM spectrum. The intensity of this radiation is a function not only of the wavelength at which it was emitted, but also of the temperature of the emitting body. Inversion of the Planck function transforms radiance values into "brightness temperatures" ($\mathbf{T_B}$) and correlates them to varying shades from white to black on a "gray scale" for purposes of image display. Thus, we see actual temperature differences between two objects as brightness differences in satellite imagery. This temperature dependence yields observable contrast between clouds and the background radiance in each respective IR wavelength band sensed.

Because surface emittance from objects can vary markedly with wavelength, retrieval of data from two identical scenes at slightly different wavelengths provides a way to locate hard-to-find features in standard single-wavelength imagery. The T_B values from one image are subtracted pixel-by-pixel from those derived from a second image in a procedure commonly known as temperature differencing. Thresholds are assigned to

the resulting difference values, and new imagery is produced, revealing new perspectives of the scene from two wavelength channels instead of one.

The capacity of the atmosphere to *transmit* the emitted radiant energy from cloud or land surface is an additional constraint affecting the end result, the ability to "see" the desired object in imagery. Figure 1 presents the transmittance spectrum of the Earth's atmosphere from ultraviolet (UV) to MW wavelengths. Satellite images are retrieved in certain "windows", or wavelength bands along the spectrum where transmittance values are most nearly equal to one. This minimizes the effects that atmospheric absorbers and emitters have on desired imagery results. Broad windows

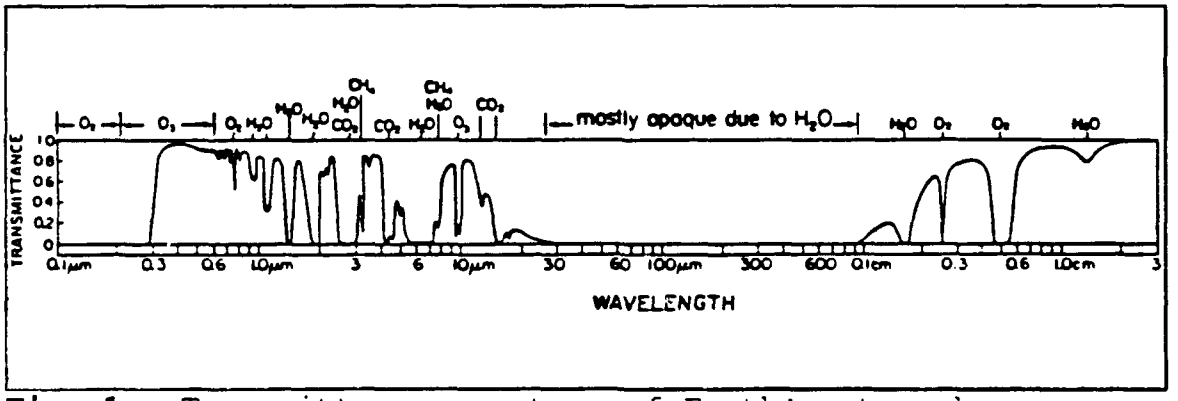

Fig. 1. Transmittance spectrum of Earth's atmosphere. [Adapted from Goody and Yung (1989).]

at this scale in Fig. 1 are seen from about 0.3 to 0.7 μm and 8 to 12 μm in the visible to IR range and from roughly 0.1 cm to longer wavelengths in the MW range.

Careful selection of wavelengths used for multispectral analysis will yield best results. As Fig. 1 shows, spectral transmittance values vary by wavelength according to the absorptance of respective atmospheric constituents like CO_2, O_2, and $H_2O_{(v)}$. Imaging a scene at two wavelengths which possess differing transmittance values of a particular gas will permit isolation and location of that gas. Thus, the success of spectral differencing techniques to expose various atmospheric gases relies on the absorption spectra of the gases investigated and the ability of the sensor to retrieve radiometric data at those critical wavelengths.

B. SENSOR AND WAVELENGTH SELECTION

Since the goal of this project deals with accurate location of low-level maritime clouds *at night*, the use of VIS or daylight imagery is limited to validation of cloud types and locations in particular areas and at times shortly following or before nighttime imaging. Finding the location of water vapor will also require using two sensing channels where water vapor absorption differs.

An important instrument used in temperature differencing techniques is the Advanced Very High Resolution Radiometer (AVHRR)/2, which senses emitted radiances of atmospheric components in five frequency channels (Table 1). Radiometric

data collected during the daytime in channel 3 contain emitted IR as well as reflected solar radiation; however, data

Table I. AVHRR CHANNEL INFORMATION [after Saunders and Kriebel (1988)].

AVHRR Channel	Spectral Range	Imagery Type
1	0.58 - 0.68 μm	Visible
2	0.72 - 1.10 μm	Near IR
3	3.55 - 3.93 μm	Near IR
4	10.3 - 11.3 μm	Thermal IR
5	11.5 - 12.5 μm	Thermal IR

collection during nighttime hours will yield three channels without reflectance contamination: channels 3, 4, and 5.

The spectral variation of water vapor transmittance in these channels makes them ideally suited to multispectral analysis applications of this study. The IR transmittance spectrum for water vapor is shown in Fig. 2. Transmittance in channel 3 is very nearly unity, whereas in channels 4 and 5, atmospheric transmittance of water vapor decreases with increasing wavelength. In addition to possessing retrieval capability in several useful channels, the AVHRR's imaging characteristics allow it to collect data at fairly high resolution, both radiometrically and spatially. At nadir,

this sensor can resolve 0.1° K temperature differences, with a spatial resolution of 1.1 km.

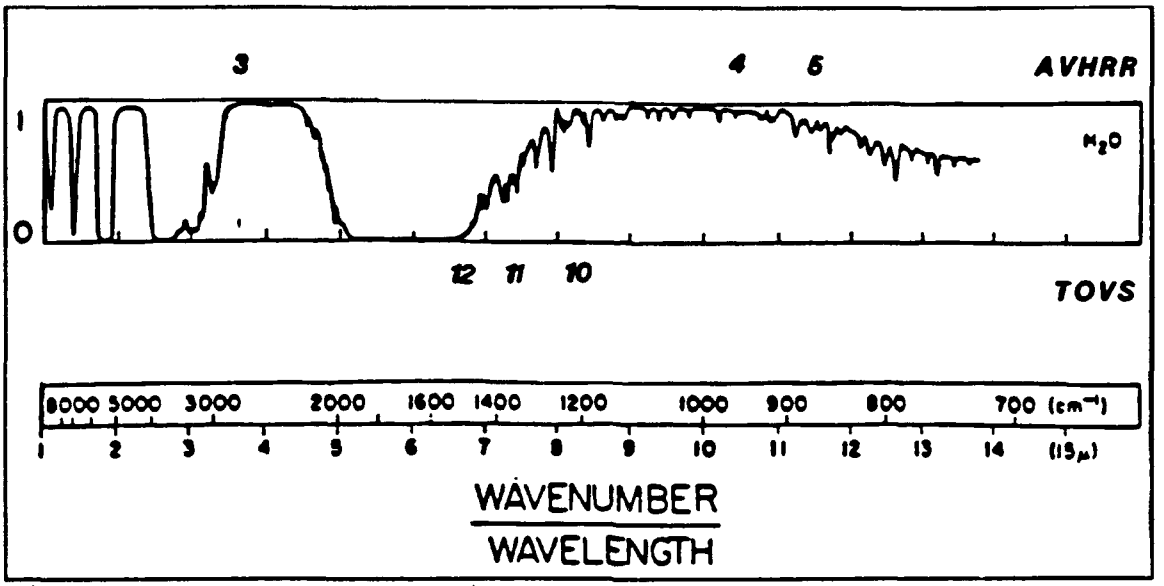

Fig. 2. Infrared transmittance of water vapor. [After Valley (1965).]

Another useful sensor for this study is the Television and Infrared Radiation Operational Satellite (TIROS) Operational Vertical Sounder (TOVS). Composed of three individual sounding instruments, TOVS retrieves temperature and moisture soundings at various wavelengths and levels in the atmosphere. One of these sounders, the High Resolution Infrared Radiation Sounder (HIRS), measures water vapor at three IR wavelengths from which images of water vapor distribution can be made. Approximate spectral locations of the three water vapor-sensitive HIRS channels 10, 11, and 12 appear below the spectrum in Fig. 2. The three IR AVHRR channels are indicated above the spectrum. Other channels on HIRS can produce VIS

and IR images from its soundings. The nadir resolution for HIRS products is 17.4 km, considerably less than the AVHRR products. For this reason, TOVS images are valuable in giving a more qualitative means of verifying location of high relative moisture and are used as such in this project.

The HIRS water vapor channel characteristics are given by the channels' normalized weighting functions in Fig. 3. Note that the peaks in the channels' weighting functions at 900, 700, and 500 mb permit analysis of $H_2O_{(v)}$ concentrations at very low, low, and mid-atmospheric levels, respectively.

Although the spatial resolution of AVHRR and TOVS is different, advantages in using imagery from these instruments are that both sensors are located on the same satellite platforms: the National Oceanic and Atmospheric Administration (NOAA) satellites. Not only will sensing times and satellite geolocation be identical, but both sensors also use similar scanning patterns, permitting an easier comparison between respective imagery products. Due to the availability of HIRS channels in the IR range, TOVS can be used at night to roughly validate water vapor distributions from multiple wavelength imagery obtained from AVHRR.

C. MULTISPECTRAL ANALYSIS WITH AVHRR CHANNELS 3, 4, AND 5

As discussed earlier, radiant energy received by the satellite sensor in AVHRR channels 3, 4, or 5 depends primarily on the emittance characteristics of the imaged

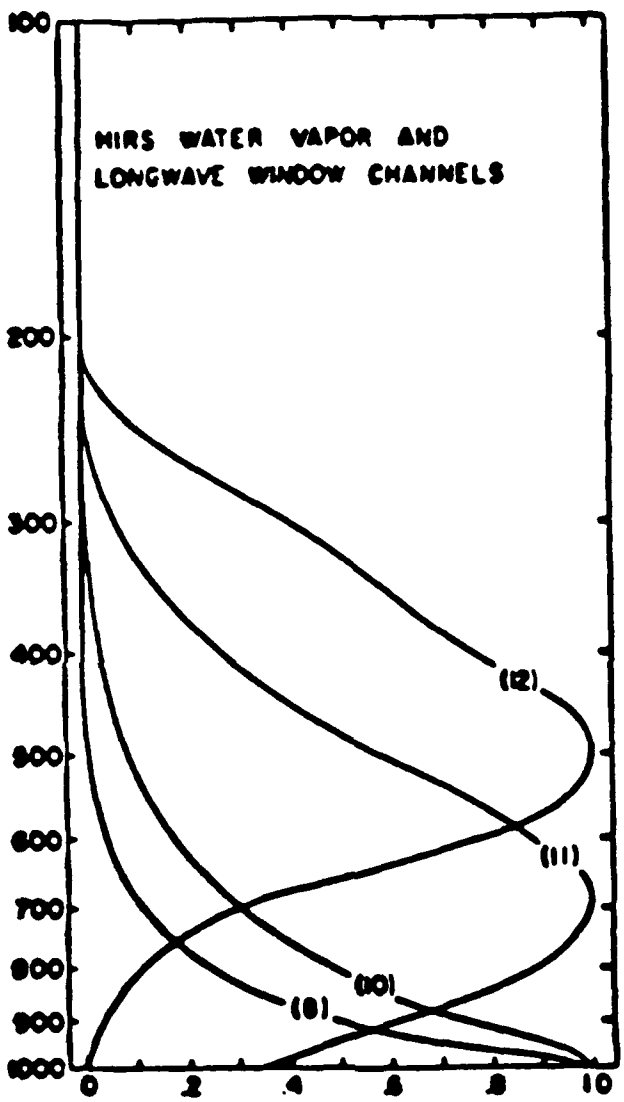

Fig. 3. HIRS $H_2O_{(v)}$ channel weighting functions (normalized). [Smith et al. (1979).]

surfaces and the transmittance of the atmosphere above those surfaces. Transmittance in any channel is a function of amount of absorptive atmospheric components between the sensor and radiant energy source. As already shown, water vapor is an absorber of radiant energy in channels 4 and 5.

Comparison of the emittance differences between cloud-free and cloudy backgrounds shows that land and sea surfaces act much more like blackbody radiators than are clouds in channels 3, 4, and 5 (Hunt, 1973). In a study of radiative properties of clouds composed of ice and water droplets, Hunt (1973) found that emittance values over clouds were consistently and significantly lower in channel 3 than in the longer-wavelength IR channels 4 and 5, which demonstrated little sensitivity to the emitting surface type. This difference makes the T_B differencing technique effective in revealing low-level clouds.

Over a cloud-free surface, emittance values in all three channels are relatively equal (Fig. 4). The lower value of emitted radiation in channel 3 from a cloud surface, seen in Fig. 5, contrasts with the much higher T_B values in channels 4 and 5 (hereafter referred to as T_4 and T_5). Thus, an algorithm designed to subtract T_4 or T_5 from T_3 would yield negative differences if cloud tops are the surface from which the radiant energy is emitted.

We assume that the clouds are of sufficient optical depth to prohibit any surface-sourced radiant energy from being

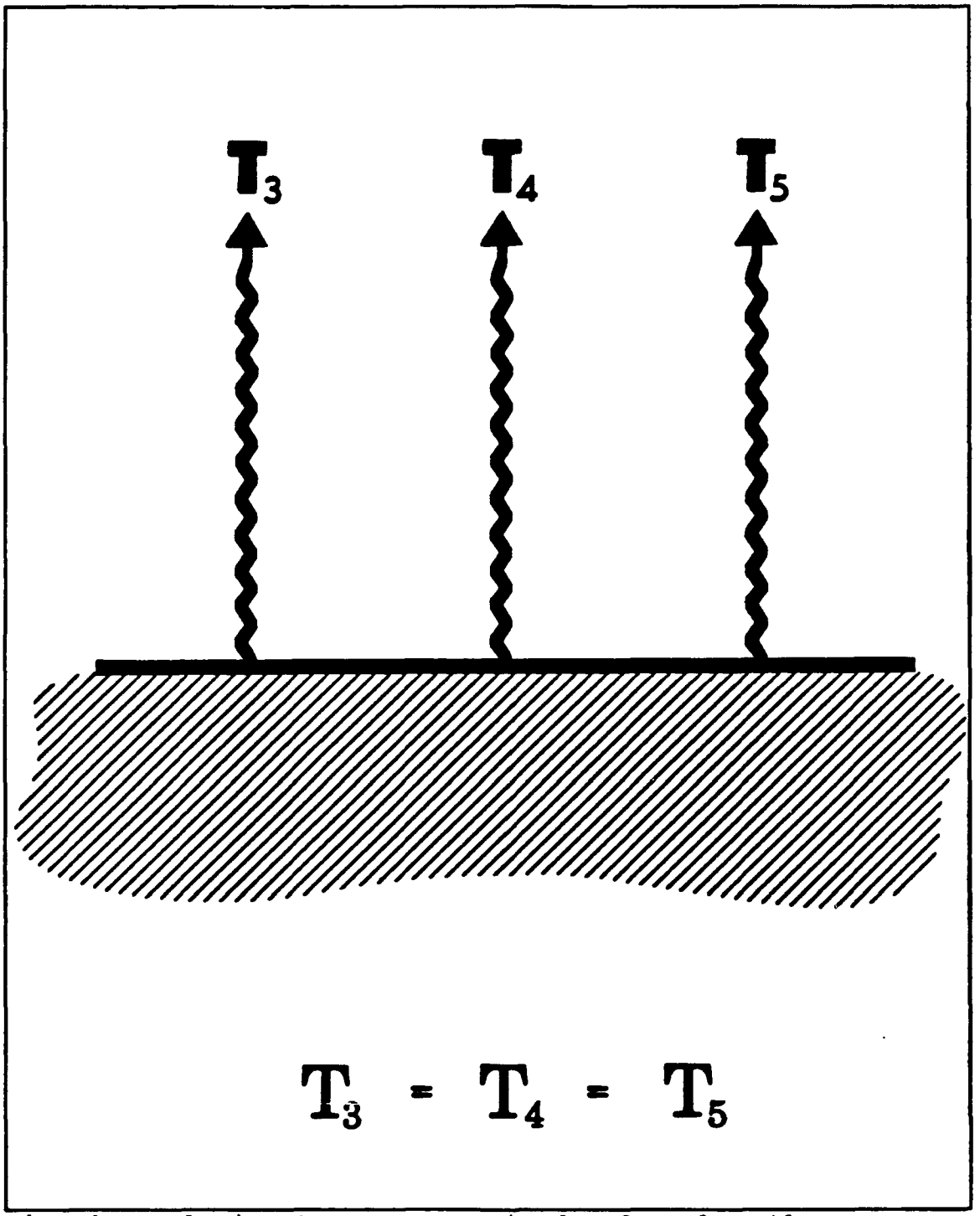

Fig. 4. Relative AVHRR T_B magnitudes for clear/dry situation.

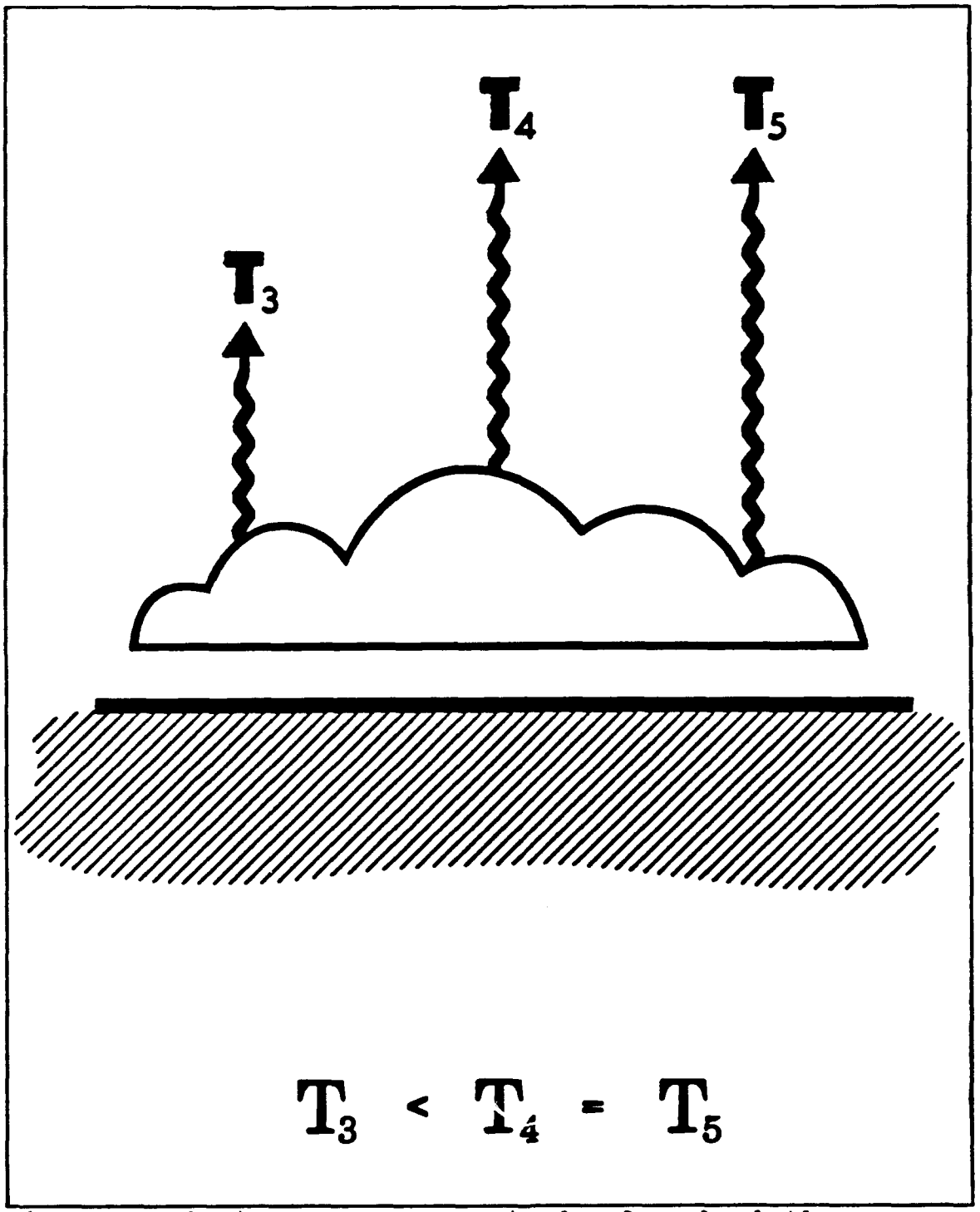

Fig. 5. Relative AVHRR T_B magnitudes for cloudy/dry situation.

transmitted through the cloud and raising the brightness temperature. This technique produced impressive results in revealing the presence of low clouds over the Bay of Fundy (Dykes, 1991). It is important to note that a higher T_B appears darker in IR imagery, as the brightness scale is inverted to show cold clouds as white. Because of this inversion technique, both thin clouds, which permit transmittance of Earth-surface emitted radiation, and mid-atmospheric emitters, which add to the radiance received by the sensor, will raise the T_B and darken the displayed signature of the object or FOV sensed.

To quantify the difference in transmittance sensitivities between the three IR channels in both dry and "moist" environments (those where water vapor was present), Dykes (1991) applied LOWTRAN7, a radiative transfer model developed by the Air Force Geophysics Laboratory. Results showed that in an atmosphere where water vapor was negligible, transmittance values for channels 3, 4, and 5 were approximately equivalent at a value nearly equal to one.

When Dykes applied the model with significant water vapor present, the respective channel moisture sensitivities appeared: all channels showed some sensitivity to the presence of $H_2O_{(v)}$, with greater sensitivity for longer-wavelength channels. Channel 5 transmittance through water vapor was roughly 67% of channel 4 values, revealing that channel 5 was the most sensitive wavelength band to the

presence of water vapor. This fact permits the use of T_B differencing between IR channels 4 and 5 to reveal the presence of water vapor in the atmosphere. Figure 6 reflects the relative magnitudes of T_3, T_4, and T_5 in the presence of water vapor over cloud-free surface. Brightness temperatures decrease as wavelength (or channel) increases due to the sensitivity of channel 4 and (especially) channel 5 to $H_2O_{(v)}$.

Adding an optically-thick emitting cloud surface in Fig. 7 reveals that T_3 has decreased considerably, mostly from the decreased emittance from the cloud top. The significant result here is that over cloud, the T_4 and T_5 relative size doesn't appreciably change. T_5 maintains its greater $H_2O_{(v)}$ sensitivity compared to T_4, and this difference can be used to *qualify* the presence of water vapor in an image.

The T_{4-5} differencing algorithm yields positive differences when water vapor is present. Depending upon the amount of water vapor present over cloud, the T_{3-4} difference will vary from near zero to large negative. Together, the T_{3-4} and T_{4-5} differences can be effective, robust tools capable of determining the effects of atmospheric water vapor and revealing low-level clouds whose low T_B contrasts keep them otherwise hidden.

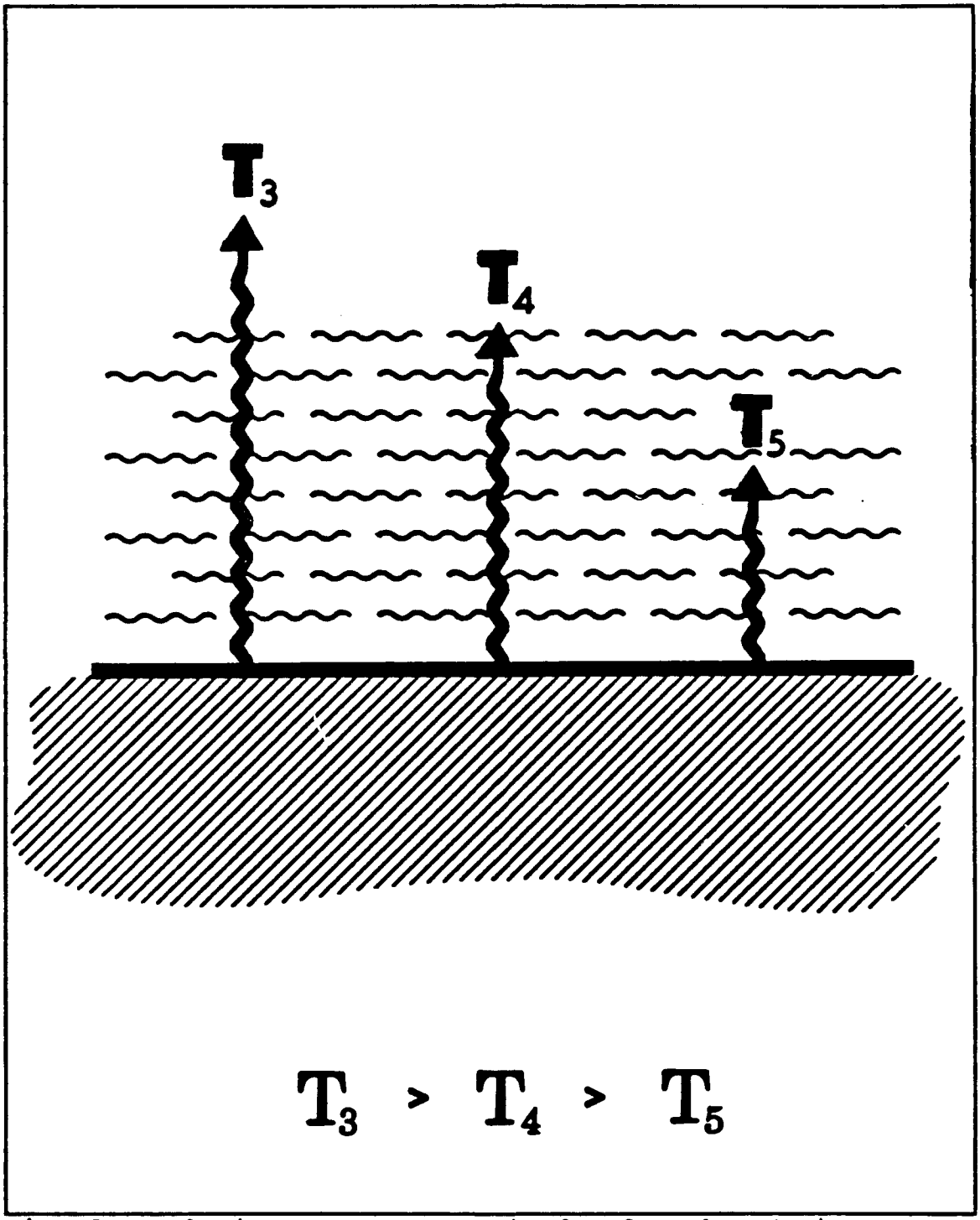

Fig. 6. Relative AVHRR T_B magnitudes for clear/moist situation.

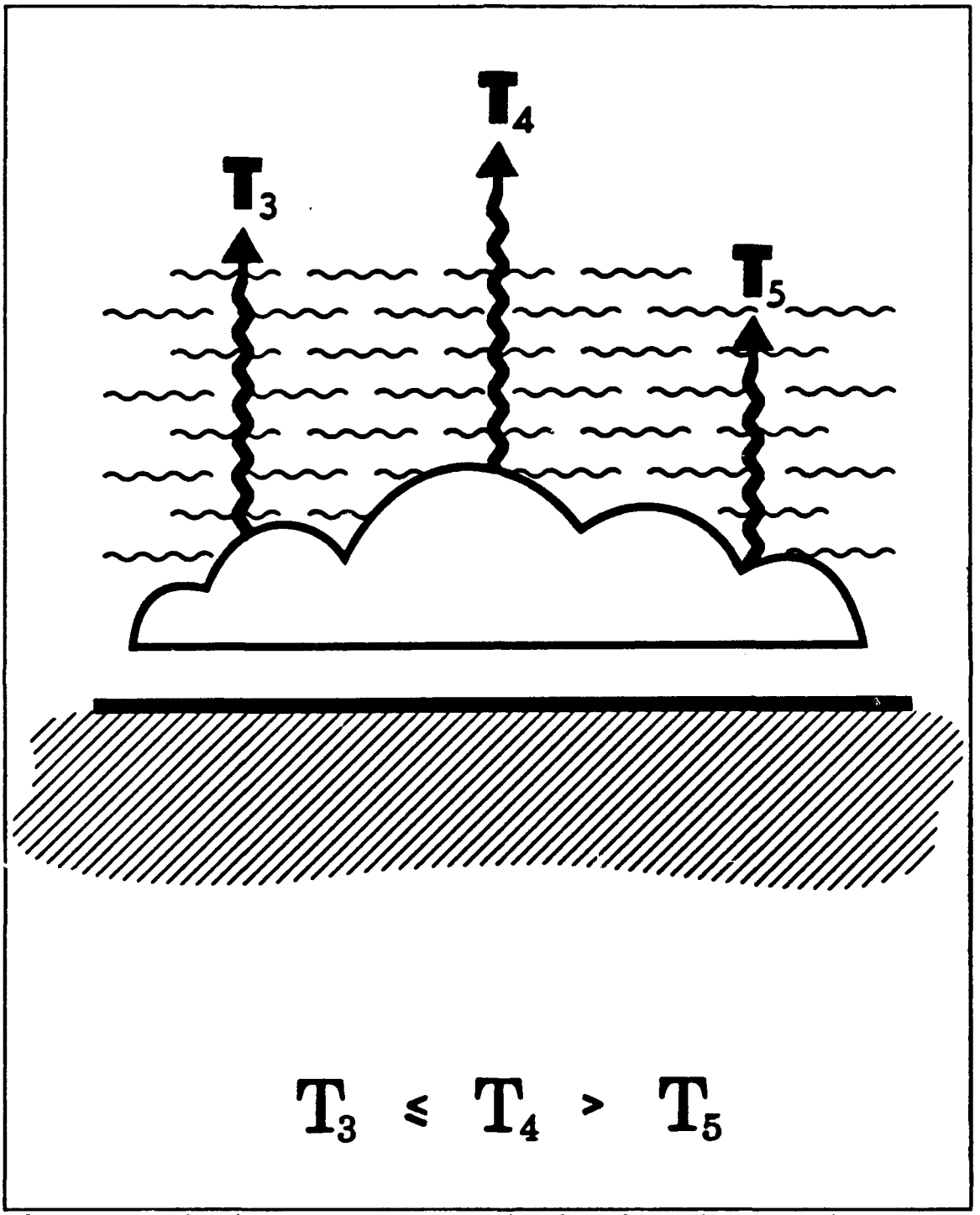

Fig. 7. Relative AVHRR T_B magnitudes for cloudy/moist situation.

III. DATA AND METHODOLOGY

A. DATA

For the purposes of this thesis, satellite imagery are restricted to areas possessing widespread low stratus over which discernible water vapor gradients occurred. Climatology of the eastern North Pacific Ocean indicates frequent occurrence of these clouds. During the late spring and summer months, vast stratus decks commonly occur west of Southern California and the Baja Peninsula related to the synoptic-scale subtropical high pressure pattern. The equatorward flow about the high pressure centers produces coastal upwelling and cool ocean temperatures under the warm subsiding air of high pressure systems.

Late season polar jet intrusions and subtropical jet stream meanders advect air masses possessing varying water vapor concentrations into this region, inducing $H_2O_{(v)}$ gradients both horizontal and vertical. As a result, the region west of Baja proved fruitful for finding areas where both cloudy and cloud-free subscenes were influenced by varying amounts of atmospheric water vapor.

Satellite imagery was obtained from the First International Satellite Cloud Climatological Project (ISCCP) Regional Experiment (FIRE) during the summer of 1987. The

FIRE data, retrieved in a High Resolution Picture Transmission (HRPT) format, contained radiometric data from both AVHRR and TOVS sensors aboard the NOAA-9 polar orbiting satellite. Thus, data from the three AVHRR IR channels critical for this study and the water vapor validation data from TOVS were available from the same source tapes.

The satellite imagery was processed at the Naval Postgraduate School's (NPS) Interactive Digital Environmental Analysis (IDEA) Laboratory using a VAX VMS computer system with satellite navigation and image processing software. From this data collection period, two satellite passes were found which contained locations of both widespread low-level stratus and water vapor gradients, as seen in Geostationary Earth Orbiting Satellite (GOES) 6.7 μm imagery. These were passes from 1154 UTC (0454 PDT) 3 JUL 1987 and at 1051 UTC (0351 PDT) 18 JUL 1987.

Initial viewing of the imagery revealed the presence of unfiltered noise in AVHRR channel 3 during this FIRE data collection period. The resulting interference patterns made the efforts to obtain results more difficult, as the noise signatures appeared in all T_{3-4} products.

1. Case 1: 3 July 1987

The satellite passes in both cases 1 and 2 were initially processed to show the channel 4 IR (thermal) signatures. Case 1 revealed a sizeable bank of low clouds off

the California coast, extending from about 40° N. to 28° N., with few clouds farther south. A thin, arc-shaped clear area bisected this cloud bank, with the northern tip just west of San Francisco Bay and the southern extent well to the southwest, as shown in Fig. 8. GOES imagery verified the presence of these features in both concurrent IR and later visible imagery.

From this overview, four subscenes were selected for further analysis: two over a mostly cloudy background (subscenes 1 and 3), and two in apparently cloud-free areas (subscenes 2 and 4), although subscene 3 possessed both clear and cloudy areas, providing a potentially valuable site for investigating water vapor effects at cloud boundaries.

2. Case 2: 18 July 1987

Three subscenes were selected for further analysis in the satellite overview for case 2, shown in Fig. 9. A predominant weather feature in this channel 4 overview was the spiral bands associated with Tropical Storm Dora, southwest of the Baja Peninsula. Clear regions occurred to the outside of the spiral convection bands, and away from the storm center to the north, where subsidence could be expected. Southwest of the border between California and Mexico, a mass of low clouds persisted from the coast to the western edge of the satellite pass.

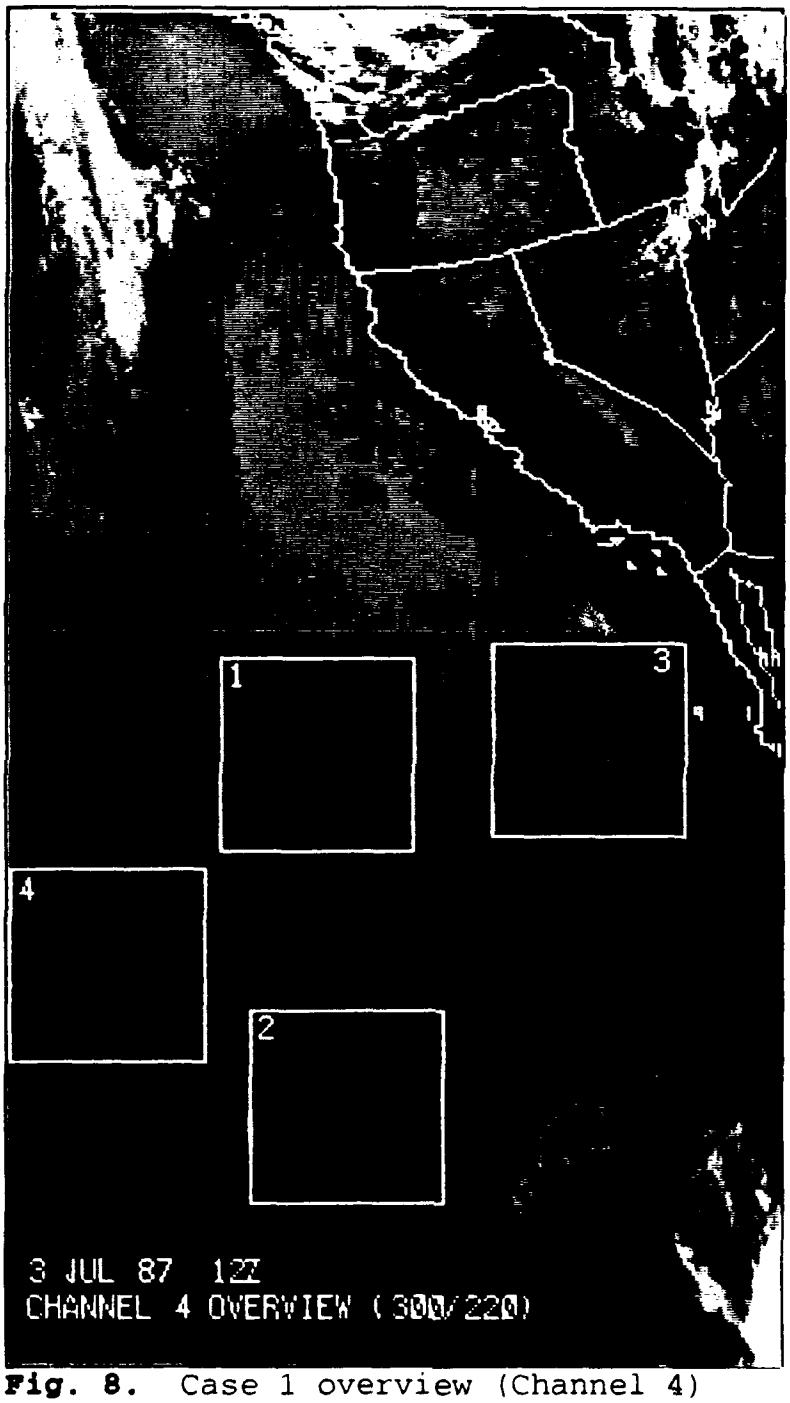

Fig. 8. Case 1 overview (Channel 4) with subscenes.

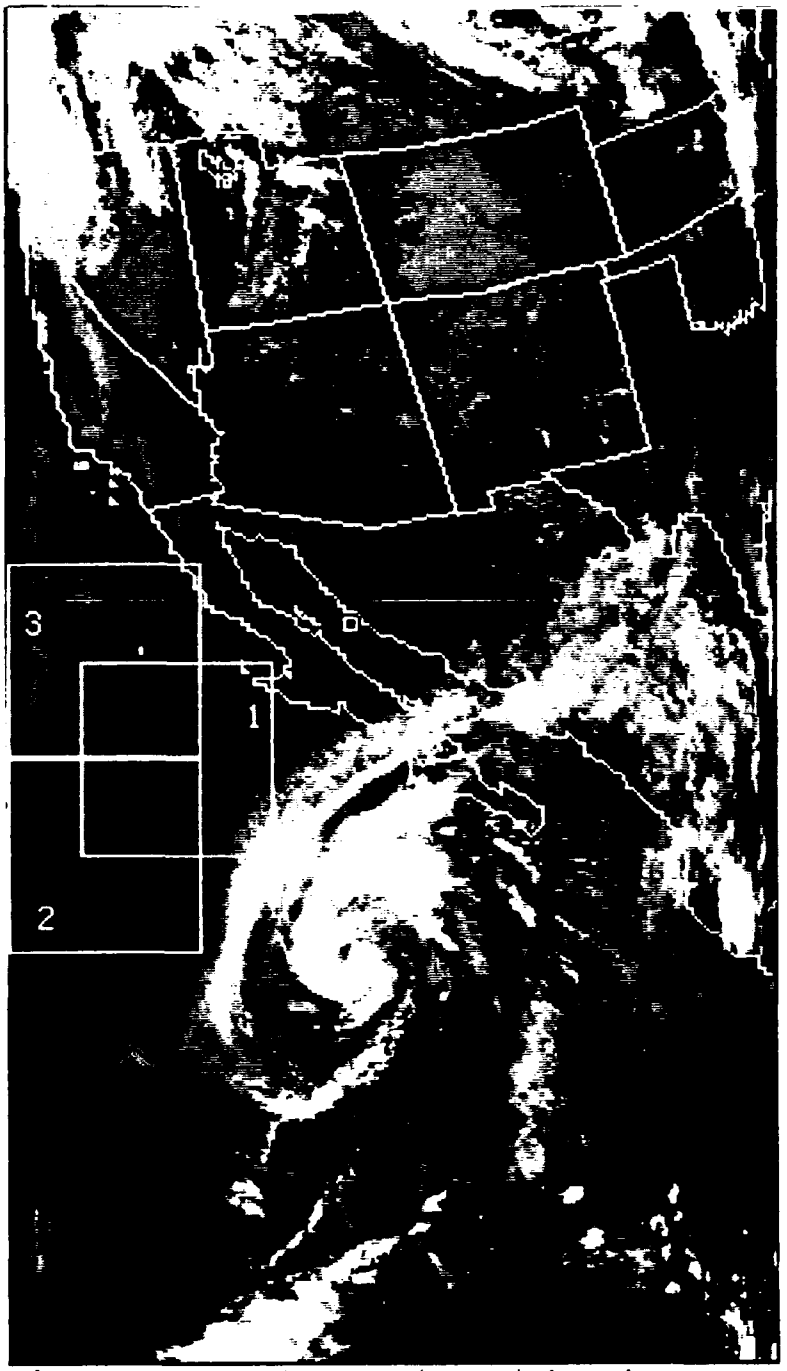

Fig. 9. Case 2 overview with subscenes.

The subscenes in this overview were initially selected for analysis of low cloud amount and possible water vapor effects in the clear and cloudy regions west of Baja. The southeast corner of subscene 1 contained some high cirrus from the T.S. outflow; the subscene spanned the clear area between the storm and low cloud deck northwest of Dora. Subscenes 2 and 3 were located at the overview edge, and in spite of some problems with distortion, appeared to contain interesting areas with cloud edges and atmospheric moisture gradients.

B. METHOD

Dykes' work (1991) in finding clouds with T_{3-4} thresholds provided the foundation from which the water vapor problem was addressed in this project. Subscene analysis proceeded by employing the spectral differencing techniques described in Chapter II for both cloud coverage and moisture or $H_2O_{(v)}$ content. The subscenes chosen in each overview contained sufficient variation in apparent cloud amount to investigate potential effects from atmospheric water vapor.

Two subscenes possessing similar cloudy backgrounds yet dissimilar moisture signatures (subscenes 1 and 2 for 3 July) offered a good opportunity for evaluating the moisture effects over cloud. Statistical techniques were applied to these subscenes in an effort to validate the cloud/moisture correlation consistent with radiative theory. Color masking of images was used to illustrate effective thresholding of

cloud/cloud-free boundaries considering moisture, and when cloudy/clear and moist/dry thresholds appeared satisfactory, other subscenes were similarly analyzed.

IV. RESULTS

The study of the water vapor effects on spectral differences required detailed multispectral analysis. Quantitative analysis of spectral differences of subscenes are used to understand the role of water vapor effects on cloud analysis and prepare better thresholds illustrated by color image masking.

A. IMAGERY ANALYSIS TO REVEAL CLOUDS AND WATER VAPOR

The multispectral analysis of case 1 and case 2 overviews using T_3 - T_4 and T_4 - T_5 differences (hereafter referred to as T_{3-4} and T_{4-5}) provided an effective way to display, respectively, cloud and water vapor distribution.

1. Analysis of T_{3-4} Imagery For Clouds

The T_{3-4} images for both cases confirmed locations of clouds seen in the channel 4 overviews (Fig. 8 and 9) and also identified clouds in areas not revealed in the channel 4 imagery. This was consistent with Dykes' results (1991). In the T_{3-4} overviews, negative differences appeared dark, indicating areas of low cloud. Lighter areas (more positive difference values) revealed clear regions. Brightest white shading indicated large positive T_{3-4} differences and showed the areas of the highest clouds composed of ice crystals.

The T_{3-4} overview for case 1 is shown in Fig. 10. In this case, two large regions of cloud appeared over the eastern North Pacific Ocean separated by a comparatively narrow clear arc in the middle of the image. Subscene 1 is almost completely filled with cloud, consistent with the cloud seen in the corresponding subscene of the channel 4 overview. Subscene 2 demonstrated the success with the T_{3-4} differencing which Dykes encountered: this subscene was almost completely filled with low cloud seen in the T_{3-4} overview, yet cloud top temperatures are nearly the same as sea surface temperatures in single channel 4 imagery. By comparison, the cloud pattern in subscene 3 is in better agreement with that seen in channel 4, however, and confirmed the presence of cloud in the eastern two-thirds of the subscene and the location of the clear area in the western third. Subscene 4 is most clear, located along the west edge of the pass.

In case 2 (Fig. 11), darker T_{3-4} areas west and northwest of T.S. Dora revealed low clouds, while lighter areas north, south, and east of the storm indicated clear regions. Subscene 1 in this image contained cloud in the northwest half, clear in the southeast half, and some cirrus in the southeast corner. Indication of a thin line of low cloud directly northwest of Dora's prominent northern spiral band was <u>not</u> suggested by channel 4 single wavelength imagery. Figure 9 represented an improvement in the low cloud detection. The channel 4 image of subscene 2 suggested a

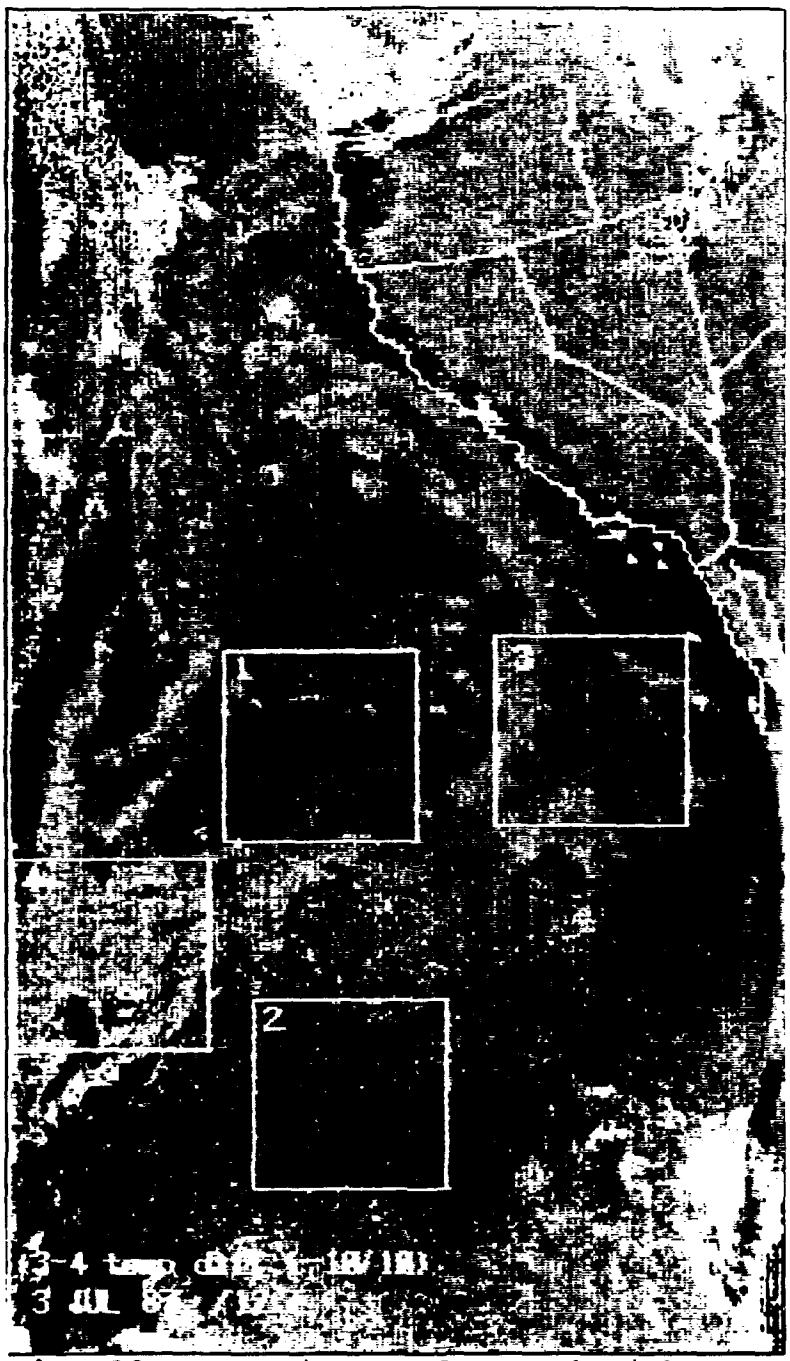

Fig. 10. T_{3-4} image of case 1 with subscenes.

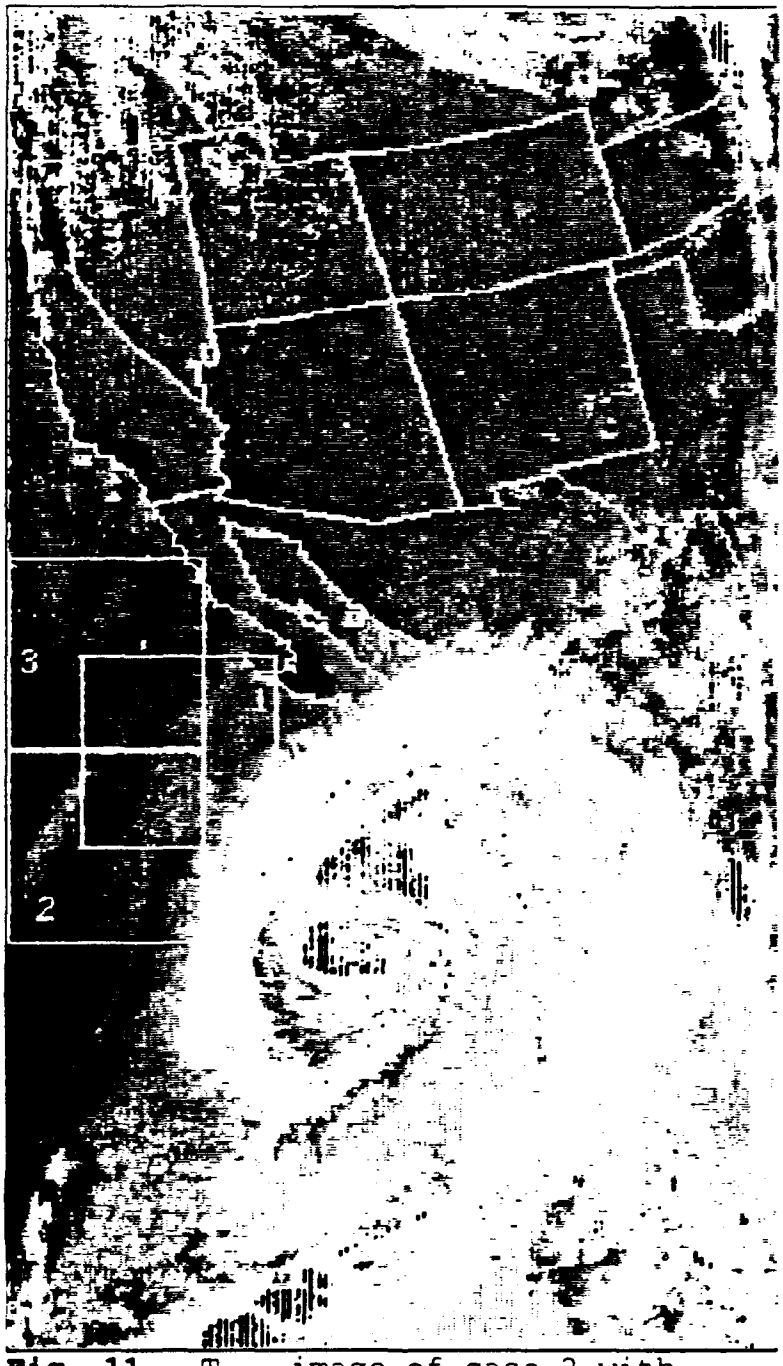

Fig. 11. T_{3-4} image of case 2 with subscenes.

fairly apparent division between clouds to the northwest and clear areas to the southeast within the box, and a wedge of cloud-free air directly north of the subscene number in the box. The T_{3-4} image confirmed the appearance of the clear wedge and the clouds to the northwest, but also revealed clouds in the southeast sector of subscene 2 which did not appear in the channel 4 overview. Finally, subscene 3 appeared mostly cloudy in both the single-wavelength channel 4 imagery and the T_{3-4} image.

2. Imagery Analysis For $H_2O_{(v)}$ Distribution

As discussed in Chapter II, both AVHRR (through multispectral methods) and TOVS channels show water vapor distribution for these two July cases.

a. T_{4-5} Imagery for Case 1

Spatial distribution of relative water vapor differences in cases 1 and 2 was displayed using the T_{4-5} imagery. Darker areas in these images indicate either small positive T_{4-5} differences or none at all due to low amounts of water vapor (dry air). More positive differences have a lighter shade by comparison, and indicate presence of greater amounts of atmospheric water vapor.

The T_{4-5} image of case 1 revealed two crescent-shaped areas of darker (drier) atmosphere in the middle of the image separated by a northeast/southwest oriented arc of moister air (Fig. 12). The southern or lower half of case 1

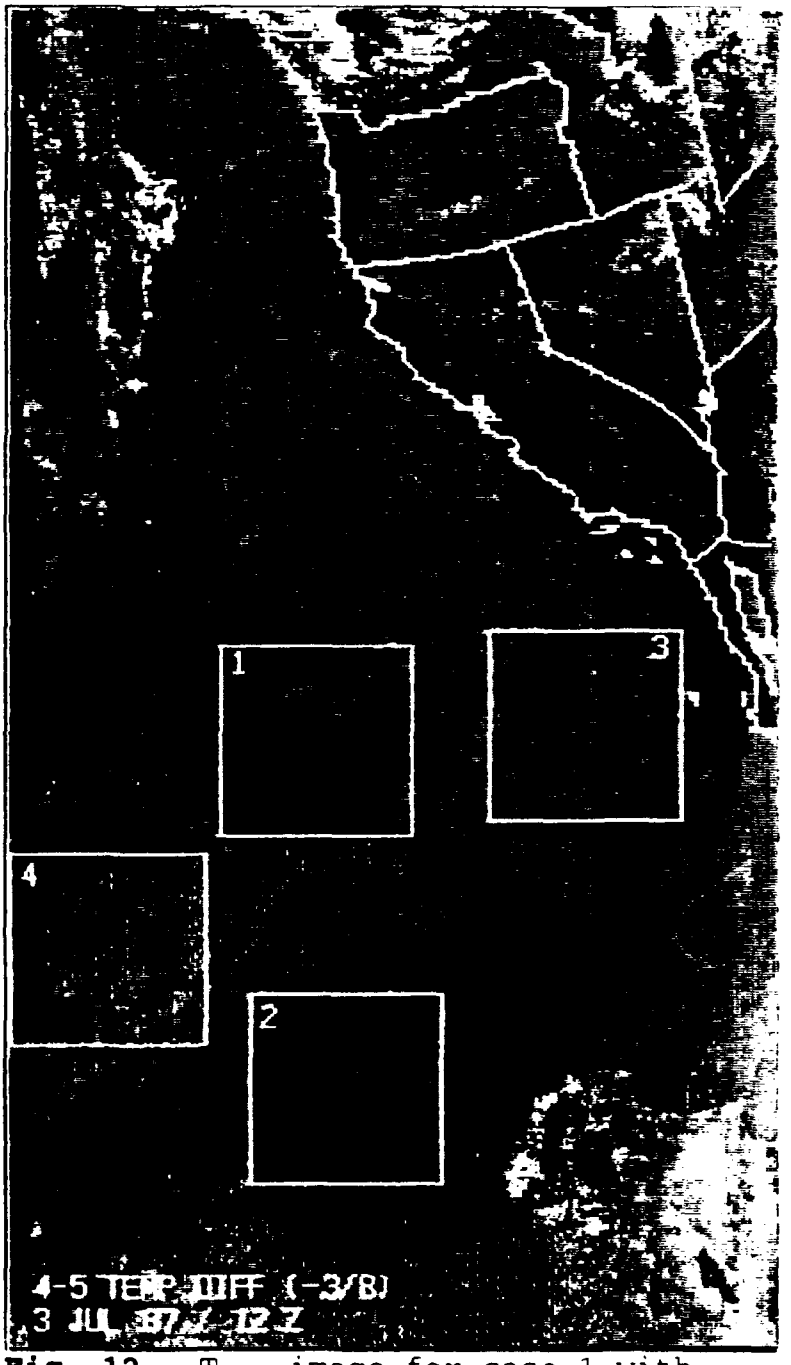

Fig. 12. T_{4-5} image for case 1 with subscenes.

appeared lighter than the northern half, indicating more moisture in that region. Here, subscene 1 appeared to be almost entirely within the darker, drier region, whereas subscenes 2 and 4 were within the moist sections of the overview. The subscene 3 moisture pattern was consistent with the pattern seen earlier in channel 4 and T_{3-4} images. The light, moist region in the western third of this subscene closely matched the clear areas shown in Fig. 9 and 10, revealing the presence of water vapor in the marine or atmospheric boundary layer.

b. TOVS for Case 1

Distribution of atmospheric water vapor suggested in spectral difference imagery was corroborated using the water vapor sensitive channels available from TOVS. Additionally, the TOVS image whose water vapor pattern most closely resembled that of the T_{4-5} image suggested the atmospheric level of the greatest T_{4-5} water vapor sensitivity. As in the T_{4-5} imagery, darker shading indicated drier atmospheric conditions, and lighter shading suggested more $H_2O_{(v)}$.

The water vapor pattern in the TOVS channel 11 image, sensitive to the low troposphere at 700 mb, appeared remarkably similar to the T_{4-5} distribution of $H_2O_{(v)}$ in (Fig. 13). In this image, subscene 1 was almost completely within a dry sector, while a radiance signature indicative of larger

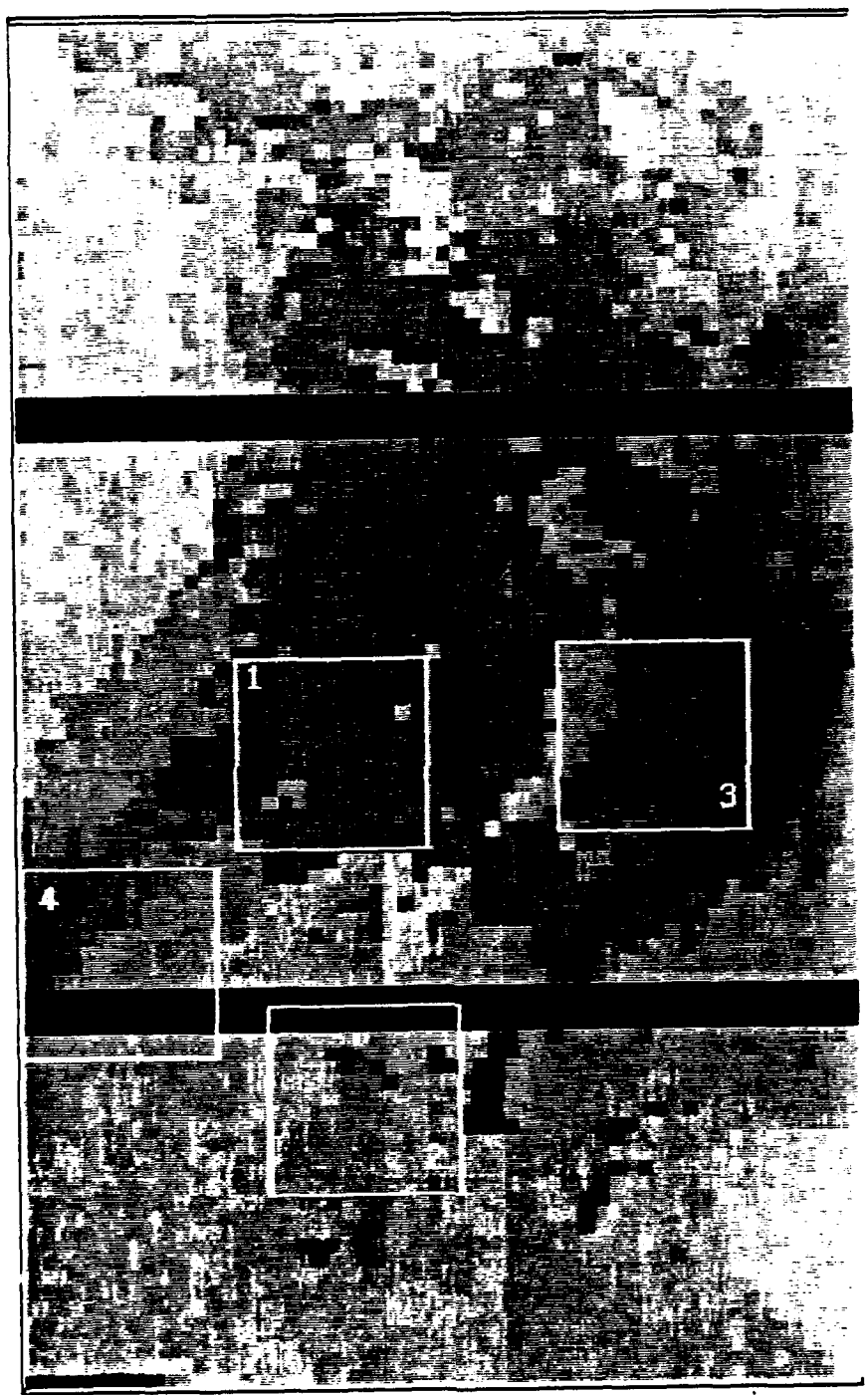

Fig. 13. TOVS channel 11 $H_2O_{(v)}$ overview for case 1.

amounts of water vapor characterized subscene 2. Subscene 3 reflected the familiar pattern for that subscene in T_{4-5}, T_{3-4}, and T_4 imagery.

By contrast, the TOVS channel 10 image of case 1, seen in Fig. 14, suggested subscenes 1, 2, and 3 were fairly dry and contained relatively similar amounts of water vapor in the very low tropospheric layers. Only subscene 4 appeared to contain less water vapor than other subscenes. The water vapor pattern from this layer did not closely resemble that seen in T_{4-5} in Fig. 12.

The TOVS channel 12 image (Fig. 15), reflective of mid-tropospheric $H_2O_{(v)}$, also showed little overall contrast in water vapor distribution throughout the overview. Although this pattern was similar to that seen in the concurrent GOES 6.7 μm water vapor imagery, it bore little resemblance to the T_{4-5} image in Fig. 12. Each of the four subscenes appeared to contain similar quantities of lighter and darker pixels.

Considering a vertical integration of horizontal $H_2O_{(v)}$ distribution over the various TOVS channels in case 1, the TOVS imagery supported the findings from the T_{4-5} image that subscene 1 contained less water vapor than did subscene 2. This supports the use of the T_{4-5} image as a reliable qualitative indicator of relative moisture differences in selected subscenes.

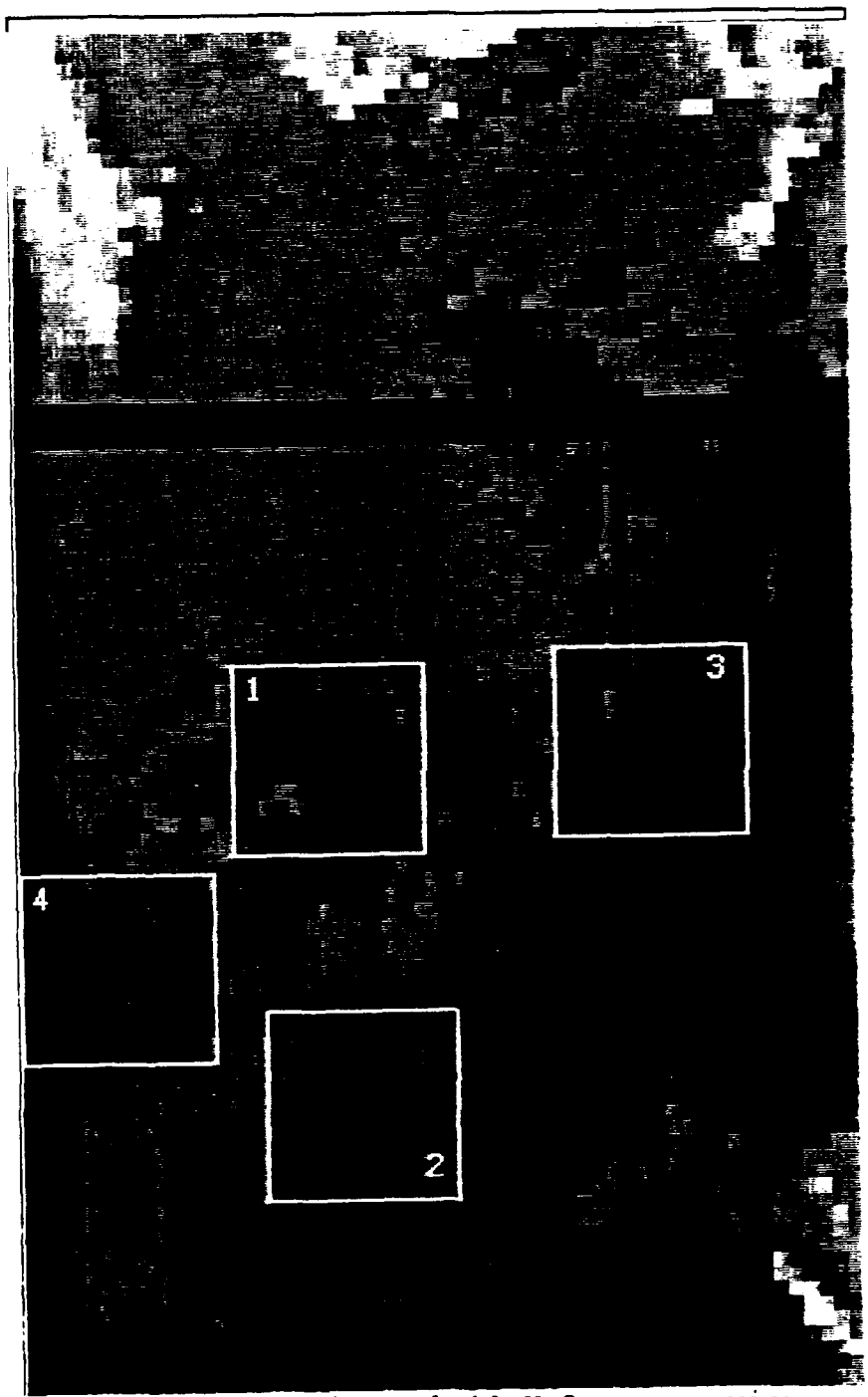

Fig. 14. TOVS channel 10 $H_2O_{(v)}$ overview for case 1.

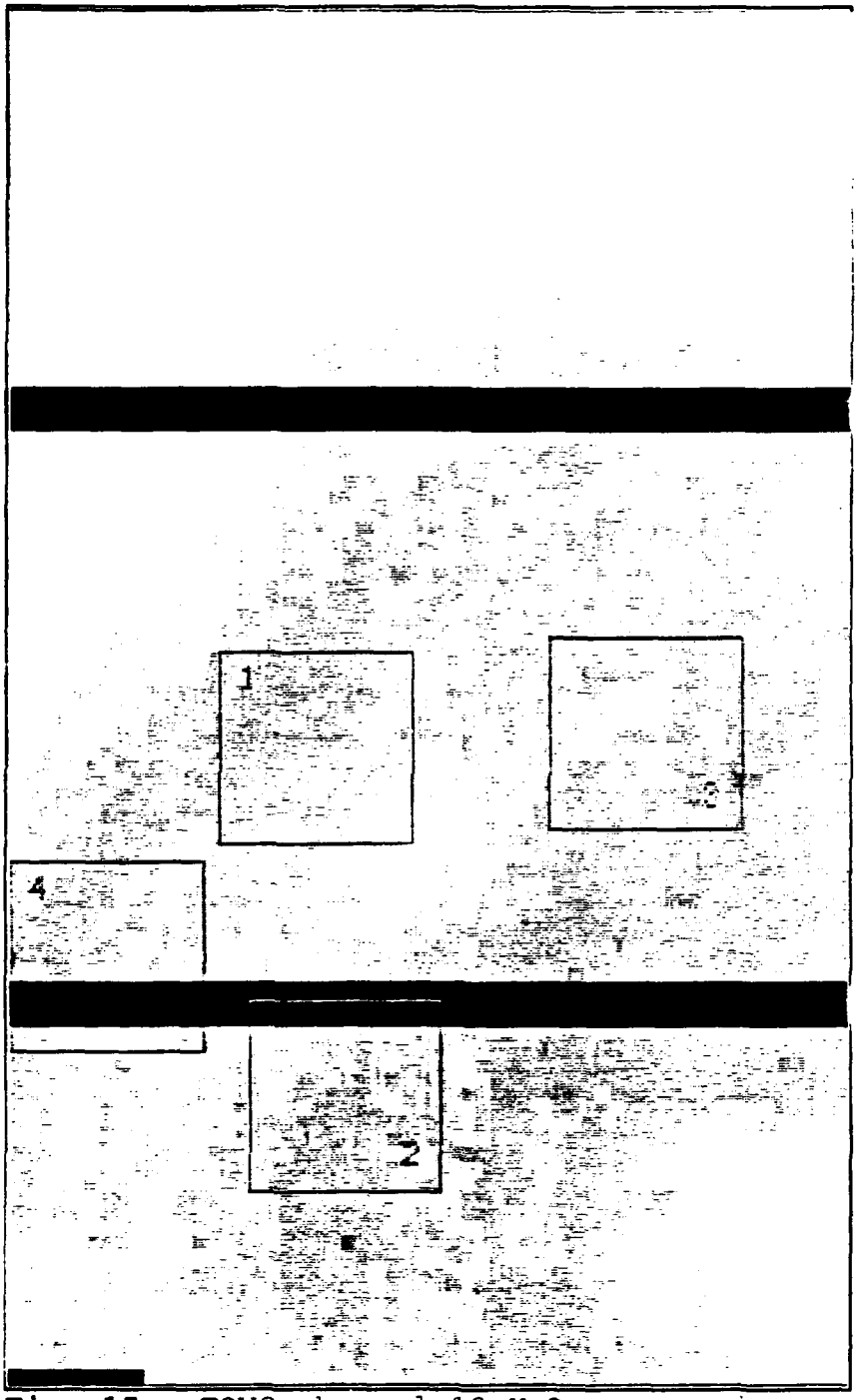

Fig. 15. TOVS channel 12 $H_2O_{(v)}$ overview for case 1.

c. T_{4-5} and TOVS Imagery for Case 2

The T_{4-5} image for case 2 is seen in Fig. 16. In this overview, a dark wedge of dry air northwest of T.S. Dora points to the northern half of the Baja Peninsula. Another filament of dry air appeared due west of the tropical storm. The TOVS imagery was examined for case 2, again indicating that the T_{4-5} image was representative of the water vapor distribution in the overview as a whole. In this instance, TOVS channel 10 produced the moisture pattern most like the T_{4-5} image, indicating the T_{4-5} image to be most reflective of water vapor at lowest tropospheric levels.

B. INITIAL ANALYSIS OF CASE 1 SUBSCENES 1 AND 2

On a large scale, the spectral difference imagery highlighted the cloudy/clear and moist/dry regions of the cases examined. In case 1, subscenes 1 and 2 contained largely homogeneous banks of low clouds with few breaks. However, the atmosphere over clouds in subscene 1 was drier than that of subscene 2. These findings suggest subscenes 1 and 2 as good candidates for quantifying the role of water vapor in spectral differencing.

Examination of the effect of varying water vapor amounts over similar cloudy backgrounds required direct comparison of the spectral difference data (both T_{3-4} and T_{4-5}) in subscenes 1 and 2. The subscene 1 and 2 pixel values in the T_{3-4} and T_{4-5} images were converted from gray shades to calibrated

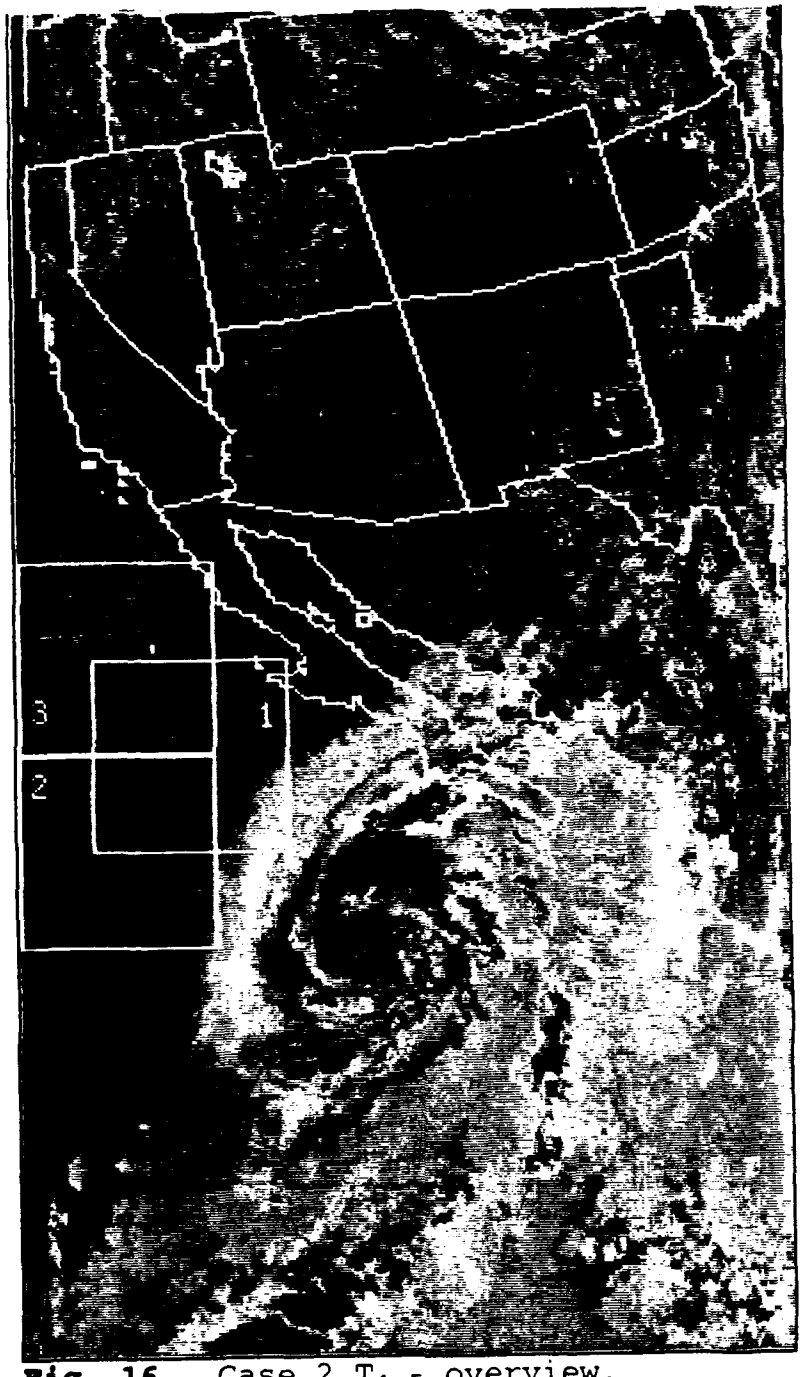

Fig. 16. Case 2 T_{4-5} overview.

temperatures and plotted against each other in two-dimensional scatter charts, seen in Fig. 17 and Fig. 18.

In these diagrams, the T_{3-4} values were plotted with respect to the Y-axis, while T_{4-5} values were plotted along the X-axis. Negative T_{3-4} values, indicative of radiance retrieved over cloud, appeared in the lower half of the graph. Positive T_{4-5} values, suggesting presence of water vapor, appeared on the right side of the chart.

Several features in these scatter plots were immediately apparent. The scatter of points for both subscenes appeared as elliptical or oval-shaped masses near the center of the plots. The major axes of these ellipses were oriented in a lower left to upper right configuration, implying a positive correlation between presence of water vapor and likelihood of a pixel to register more of a cloud-free signature than a cloudy one. Additionally, both clusters occurred mostly below the T_{3-4} zero line, confirming that both subscenes were predominantly cloudy. The scatter of both masses of points appeared to be in the positive T_{4-5} sector, generally with difference values of +1° K or less, revealing that quantitative moisture differences between the two subscenes were not large.

Comparison of the scatter plots as a whole showed the mass of data points for subscene 1 shifted up and to the right in subscene 2, again suggesting the positive T_{3-4}/T_{4-5} correlation as a cloudy, dry scene becomes more moist. Since

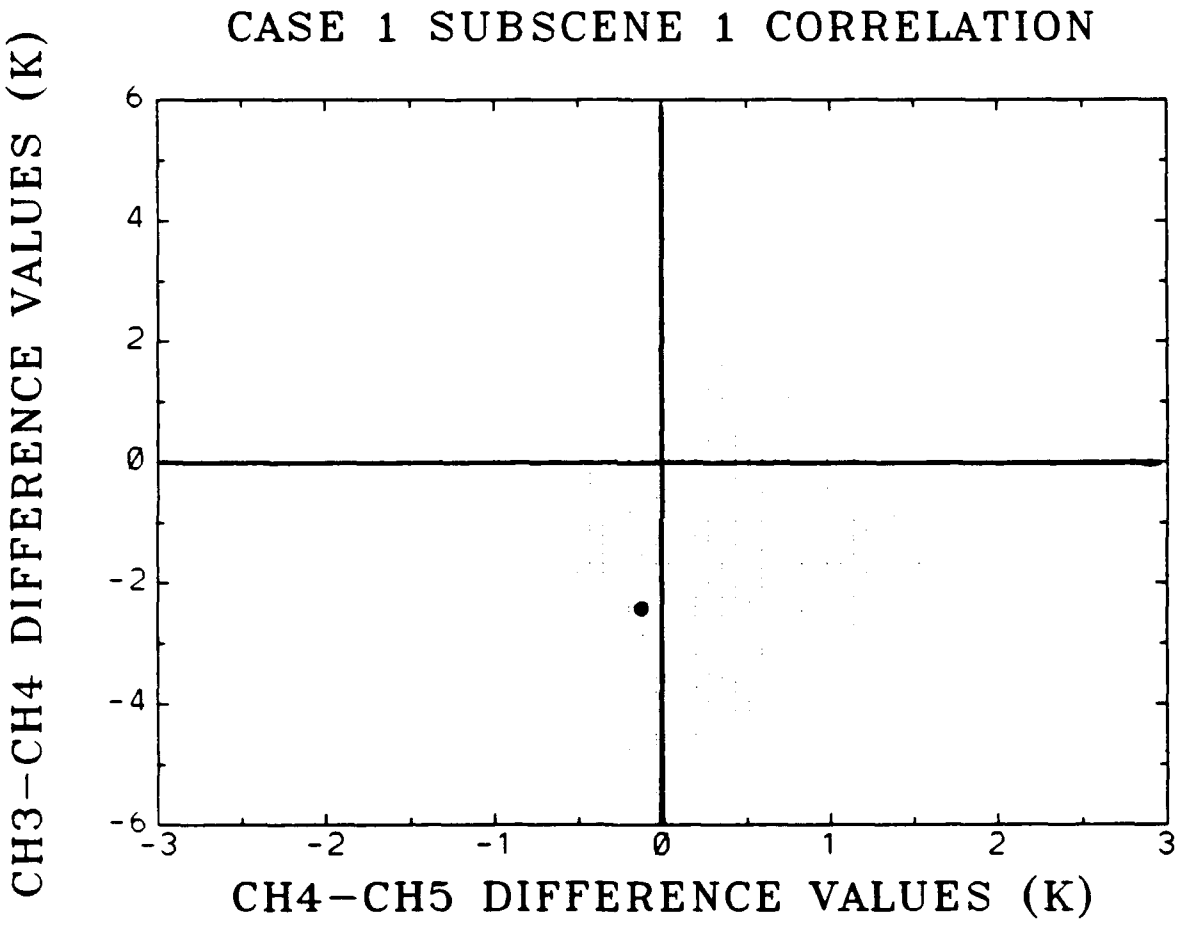

Fig. 17. T_{3-4}/T_{4-5} scatter plot for subscene 1 (cloud/dry). Units are degrees K.

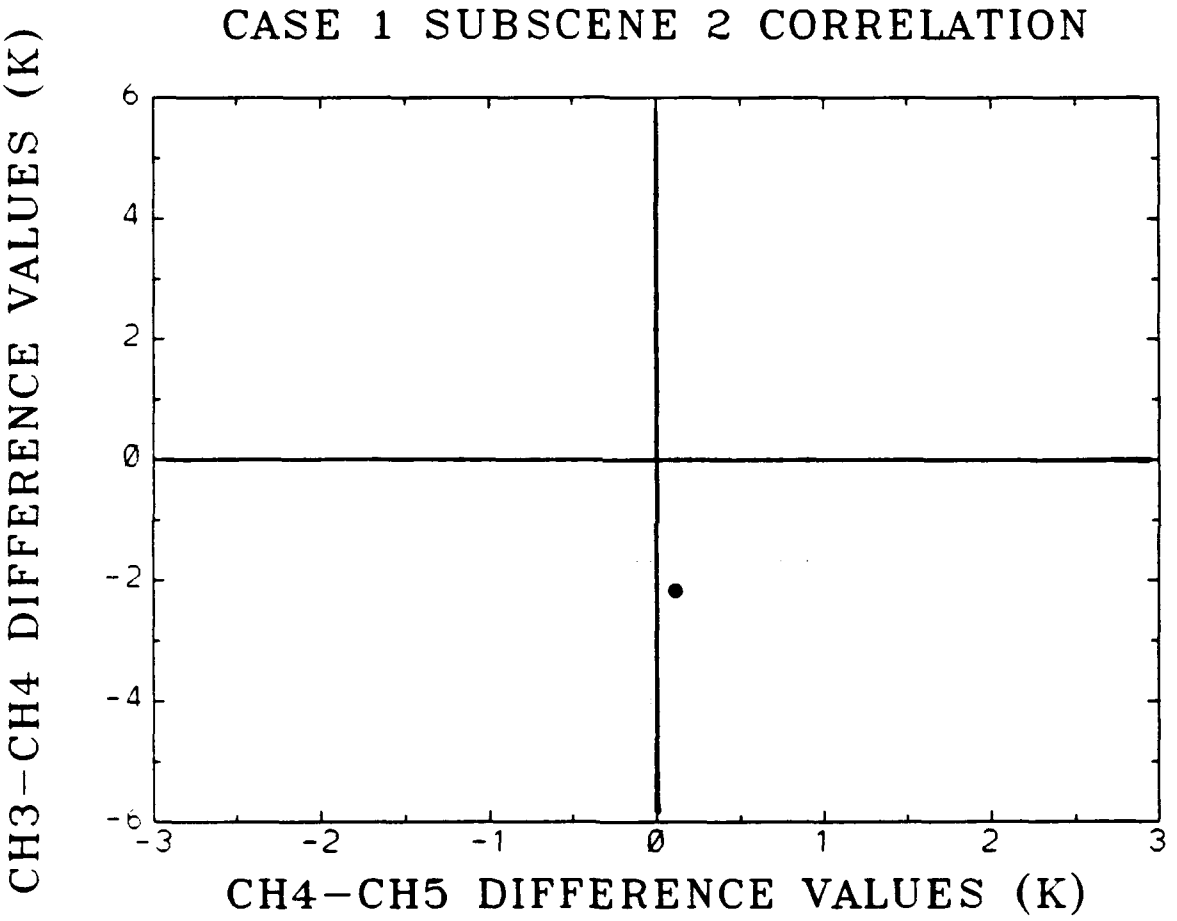

Fig. 18. T_{3-4}/T_{4-5} scatter plot for subscene 2 (cloudy/moist). Units are degrees K.

no clearly defined breaks in the scatter plot appeared, various thresholds will be tested to delineate boundaries between clear and cloud and between moist and dry radiance signatures.

C. THRESHOLD SELECTION AND ADJUSTMENT

Selection of specific T_{3-4} or T_{4-5} thresholds in the scatter plots permitted application of an image masking routine to illustrate cloud boundaries, water vapor boundaries, or combinations of both.

1. Cloud Thresholds Using Only T_{3-4} Data

The LOWTRAN model in Dykes' work (1991) suggested threshold values for illustrating cloud boundaries in both dry and moist cases. Dykes applied these thresholds, given by specific T_{3-4} values, but which did not include any water vapor effects, to produce color masking of imagery that was highly illustrative of hidden cloud boundaries.

When a threshold value was selected to display cloud, a graphics program would color all pixels in an image possessing that threshold value or lower. Thus, if the threshold T_{3-4} values were fairly accurate, the painted pixels would mask or portray a reasonable depiction of the cloud within an image.

Dykes determined T_{3-4} thresholds for dry and moist cases by analyzing difference values for pixels varying from overcast to clear. For his dry case, the threshold between

clear and scattered cloud in a pixel was set at -1; for the moist case, it was found to be zero.

Since subscenes 1 and 2 in case 1 contained mostly cloud, the clear areas, not the clouds, were masked yellow using the initial thresholds mentioned. For purposes of comparison with the single-wavelength imagery, color enhanced channel 4 images for the two subscenes are presented with yellow representing clear regions based solely on thermal IR signatures, and not with the use of multispectral differencing. For these two subscenes, there is sufficient temperature difference between the sea surface temperature and cloud top to accurately map most low cloud areas.

Figure 19 displays the subscene 1 mask for all points seen in the scatter plot having a T_{3-4} value greater than or equal to (-1). It is evident in Fig. 19 that this threshold rendered as clear (yellow) many pixels which were obviously cloudy. Also, some of the peak amplitude values in the noise were classified as clear. Additionally, the pixels at or near the true cloud boundaries reflected larger clear areas than in fact exist. Despite the noise and the problem of the mask classifying some cloud as clear, the truly clear areas were located where the colored pixels were concentrated.

Figure 20 displays a T_4 image of the same subscene. It is color enhanced to display clear areas as yellow and cloud-filled pixels as red, based upon a subjective evaluation of the image under magnification. Pixel values were obtained

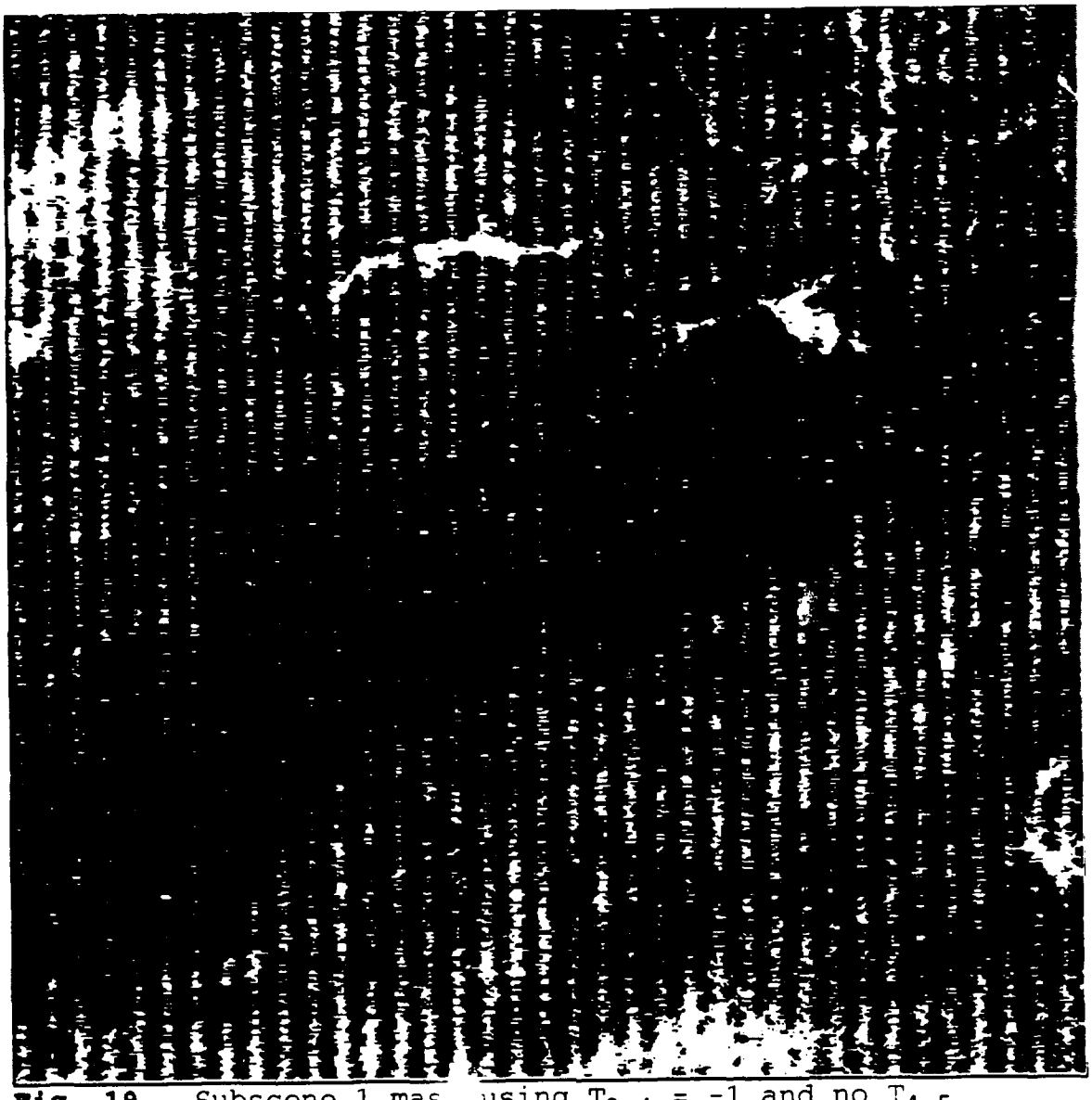

Fig. 19. Subscene 1 mas using $T_{3-4} = -1$ and no T_{4-5} threshold value. Yellow indicates cloud-free regions.

Fig. 20. Subscene 1 channel 4 color enhancement. Red indicates cloud; yellow reveals clear areas.

in distinctly clear and cloudy areas, as well as from regions where true cloud boundaries were less apparent. Those values implied a pixel value threshold between clear and cloud, and the image was colored accordingly. The color enhancement corroborated the locations of greatest confidence of clear air in Fig. 19 without the unwanted noise effects. An advantage in using this enhancement is that the enhancement threshold is empirically derived, providing a very close approximation to the areas where truly cloud-free pixels are found, since a difference in cloud top and sea surface temperatures is present.

For subscene 2, a T_{3-4} threshold value of zero is used, shown in Fig. 21. This displays as clear air (yellow) those points in the scatter plot having T_{3-4} values of zero or greater, which was the moist-case threshold Dykes used. The higher-value threshold applied to this moister subscene plainly masked many fewer pixels as clear. Although some noise contamination was apparent in the upper right corner of the image, the algorithm capably masked the shapes of clear areas at the top of the subscene. The color-enhanced channel 4 subscene (Fig. 22), created like Fig. 20, supported the masking results in this region. Two areas containing cirrus clouds, along the upper left and middle right subscene edges, were masked as clear because the T_{3-4} values were higher than the threshold.

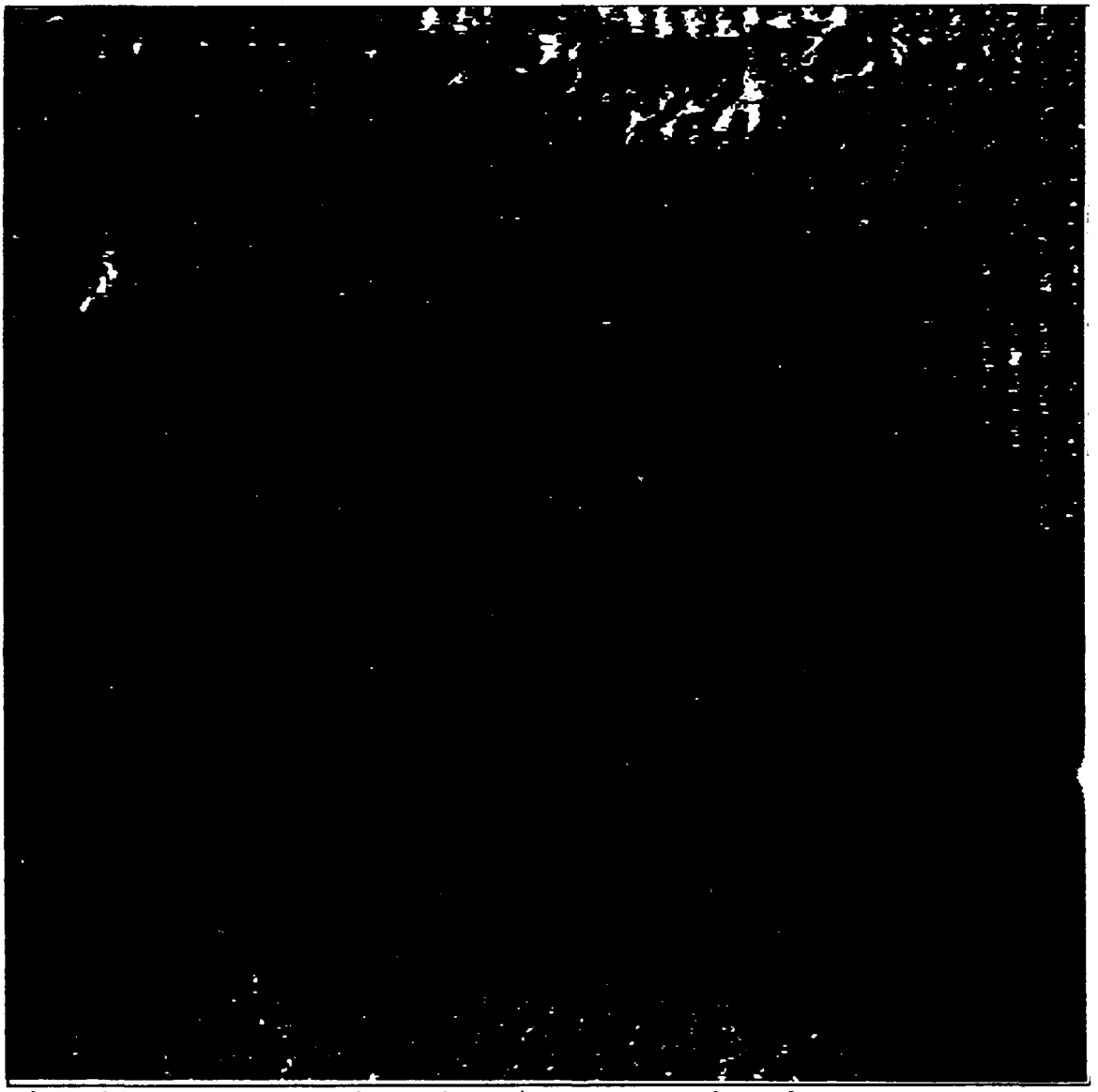

Fig. 21. Subscene 2 mask using $T_{3-4} = 0$ and no T_{4-5} threshold value. Yellow indicates clear regions.

Fig. 22. Color enhanced channel 4 image of subscene 2. Red shows clouds; yellow reveals clear areas.

The masked T_{3-4} image also revealed smaller clear areas near the subscene bottom compared to similar regions in the color enhancement, T_4. Enhancements of this T_4 image revealed cloud patterns consistent with the masking results, as did examination of the T_{3-4} image. Careful analysis of the T_4 image under magnification revealed a cloud/cloud-free threshold at the image top that differed from the "best" threshold at the image bottom. When the threshold was applied that most correctly colored the clear areas at the image top, significant numbers of visibly cloudy pixels at the image bottom were colored yellow, indicating clear air. Conversely, the most suitable threshold for accurate enhancement of the clear areas at the subscene bottom left some clear areas at the top uncolored.

In addition to suggesting a very slight temperature difference between cloud edge and sea surface temperature in this region, the results of the mask in Fig. 21 also suggest that the spectral difference (T_{3-4}) image was effective in revealing true cloud edges that single-channel imagery would indicate as clear.

2. Addition of T_{4-5} Thresholds

A review of the subscene 1 and 2 scatter plots (Fig. 17 and 18) revealed many points in each subscene falling to the left of the T_{4-5} axis, reflecting negative T_{4-5} differences. The radiative theory in Chapter II indicates a

T_{4-5} difference could only be zero in air with no water vapor present, since T_5 is never greater than T_4 for the cloud/water vapor problem addressed here.

Several possibilities exist to account for the presence of these pixels in negative T_{4-5} ranges. Most likely, the spectral variations in the emitting surfaces allow T_5 to register higher than T_4. For clouds, difference in the cloud droplet size spectra could explain these phenomena. This suggests setting the T_{4-5} cloud threshold at zero. Areas with $T_5 > T_4$ will be classified cloud independent of T_{3-4} threshold.

In Fig. 23, the addition of a T_{4-5} threshold of zero to the dry case T_{3-4} threshold of (-1) slightly improved the analysis of the clear areas. Significantly less noise contaminated the results. Consequently, the location of the cloudy/cloud-free areas was somewhat better defined, and affirmed the capability of spectral differencing to produce reliable images.

Although the masking change in subscene 1 was noticeable, adding the moisture threshold to the mask for subscene 2 revealed little if any change. Inspection of the original scatter plots (Fig. 17) indicated subscene 1 contained a number of points in the upper-left quadrant of the diagram which were no longer masked when the T_{4-5} threshold was applied. Subscene 2's scatter plot (Fig. 18) contained

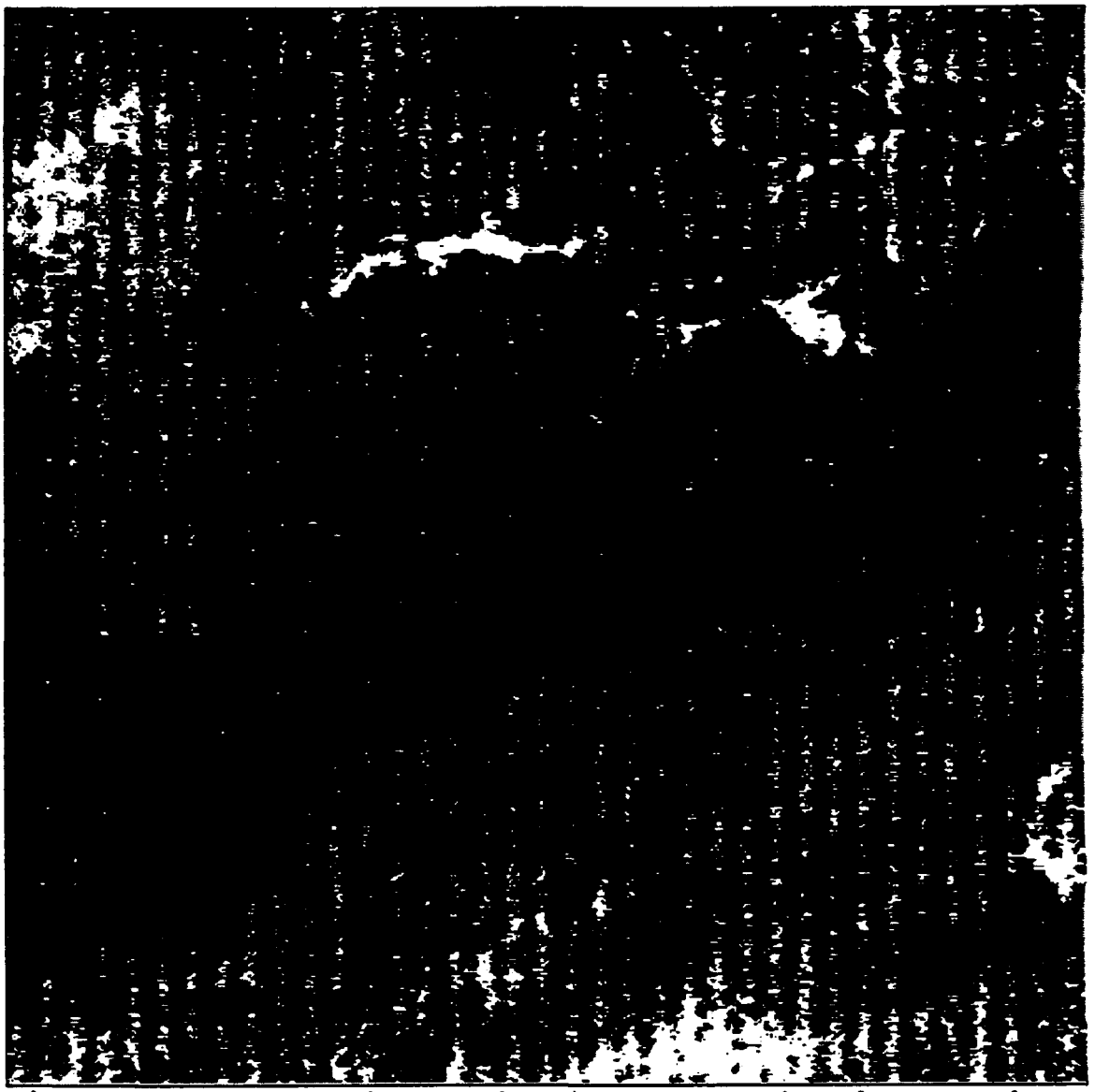

Fig. 23. Mask of subscene 1 using $T_{3-4} = -1$ and $T_{4-5} = 0$ threshold values. Yellow indicates clear area suggested by the mask.

few points in this region, explaining the relative effects on the masked images when the low T_{4-5} threshold took effect.

3. Applying $H_2O_{(v)}$ Correlation Thresholds

To improve the T_{3-4}-only thresholding, and to test the hypothesis of this thesis, additional comparisons of subscenes 1 and 2 were completed.

a. Analysis of the T_{3-4}/T_{4-5} Correlation

To determine the shift of pixels from subscene 1 to subscene 2, a histogram analysis obtained the mean T_{3-4} and T_{4-5} values in each of the two subscenes. These two values are then displayed as a black dot in Fig. 17 and 18, respectively, revealing the centroids of the two plots. In subscene 1, the centroid was just left of the T_{4-5} axis; the centroid for subscene 2 was found slightly to the right (within positive T_{4-5} values) of the first centroid, and also at a less-negative T_{3-4} location.

A linear regression analysis confirmed the positive correlation between T_{3-4} and T_{4-5} in each of the subscenes with the correlation coefficients of 0.27 and 0.33, respectively. Assuming a linear correlation between increasing T_{4-5} values and higher T_{3-4} levels as the centroid shift suggested, a straight line was drawn through the two centroids, yielding a slope of 0.45 (Fig. 24). The behavior of the pixels in these subscenes suggests applying a sloped threshold rather than a constant line of zero slope, as some

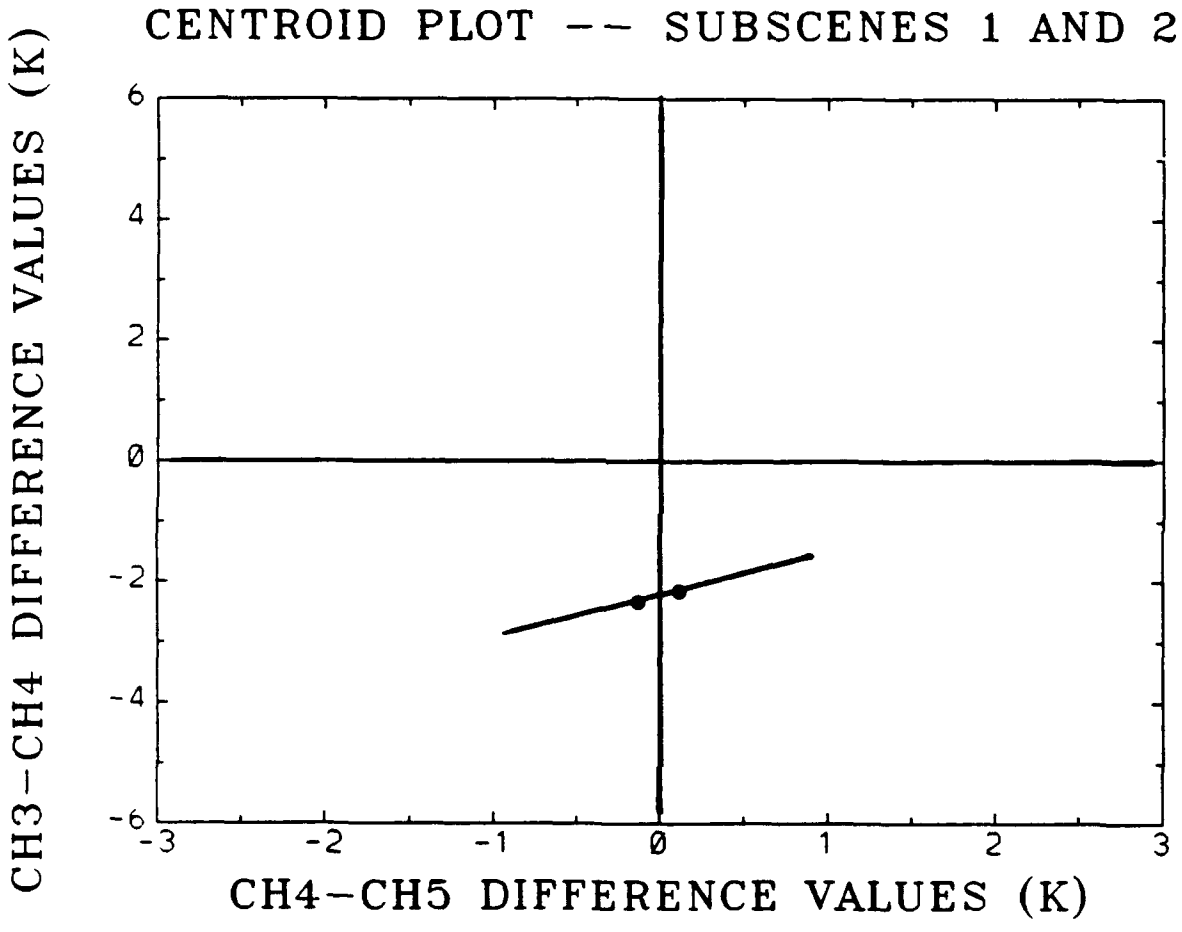

Fig. 24. Threshold slope derived through centroids of subscenes 1 and 2.

pixels possessing higher T_{4-5} values and initially identified as clear could be reclassified as cloudy, consistent with the demonstrated relationship derived from subscenes 1 and 2.

b. Threshold Refinement in Subscenes 1 and 2

Reexamination of the subscenes using the sloped thresholds improved upon the thresholds obtained in Dykes' work. Figures 25 and 26 show results of a classification scheme applied to the scatter plots of subscenes 1 and 2. Pixel values were obtained from the same location of T_{3-4} and T_{4-5} imagery for the two subscenes. Based upon the T_4 pixel value and subjective analysis, the pixel was judged to be either cloud-free, cloud-contaminated, or indeterminate due to problems with resolution. The resultant classified pixels are plotted on the scatter diagram.

In subscene 1, this secondary classification revealed the clear pixels restricted to a V-shaped wedge in the upper-right corner of the scatter. Pixels having an identifiable cloud signature (whether overcast, broken, or scattered) were logged as cloudy, and attained a high T_{4-5} value of 0.27 in the positive T_{3-4} region, an area where cloud would not normally be expected. Pixels in clear air were found having negative T_{3-4} values as low as -1, which indicated the initial Dykes threshold as a reasonable first guess for this cloudy/dry scene.

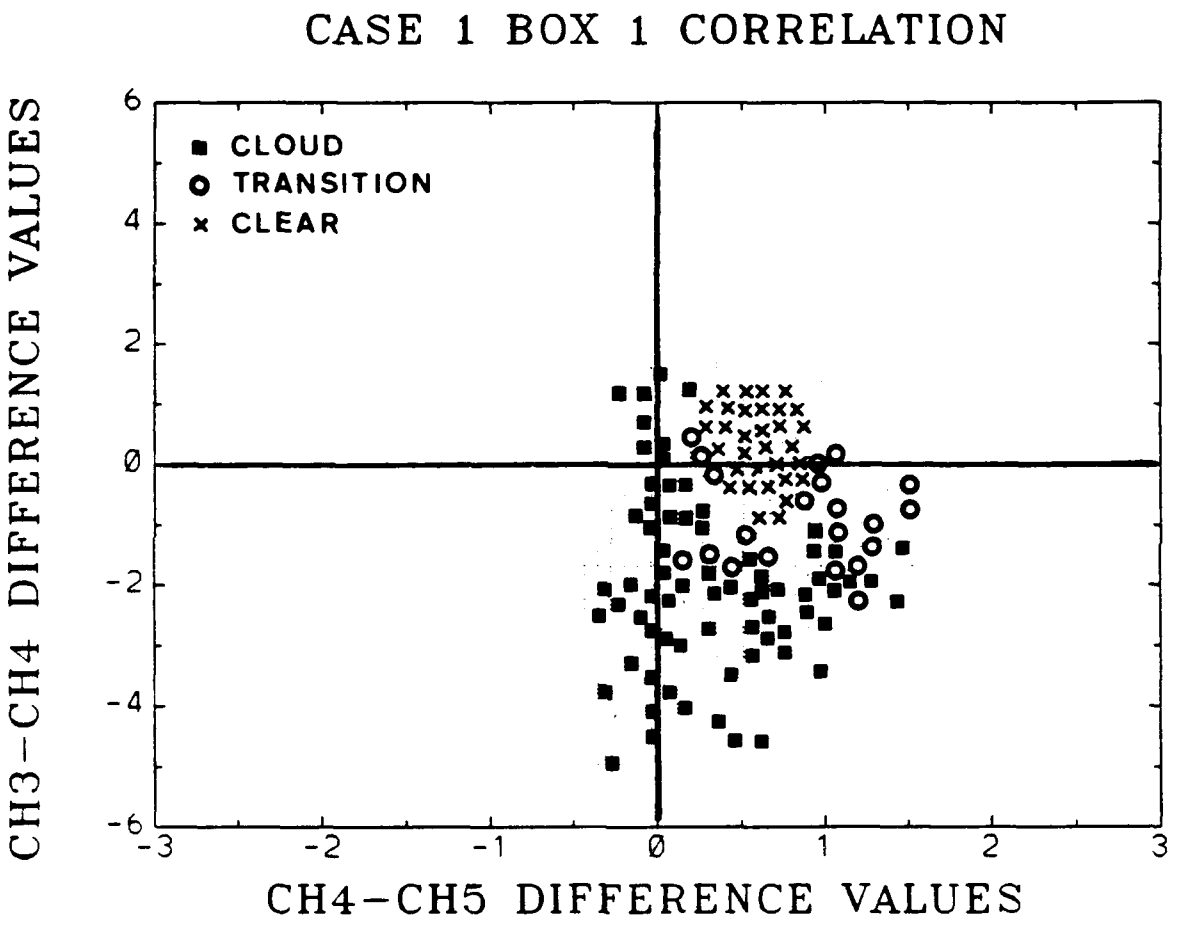

Fig. 25. Case 1, subscene 1 scatter plot reclassification.

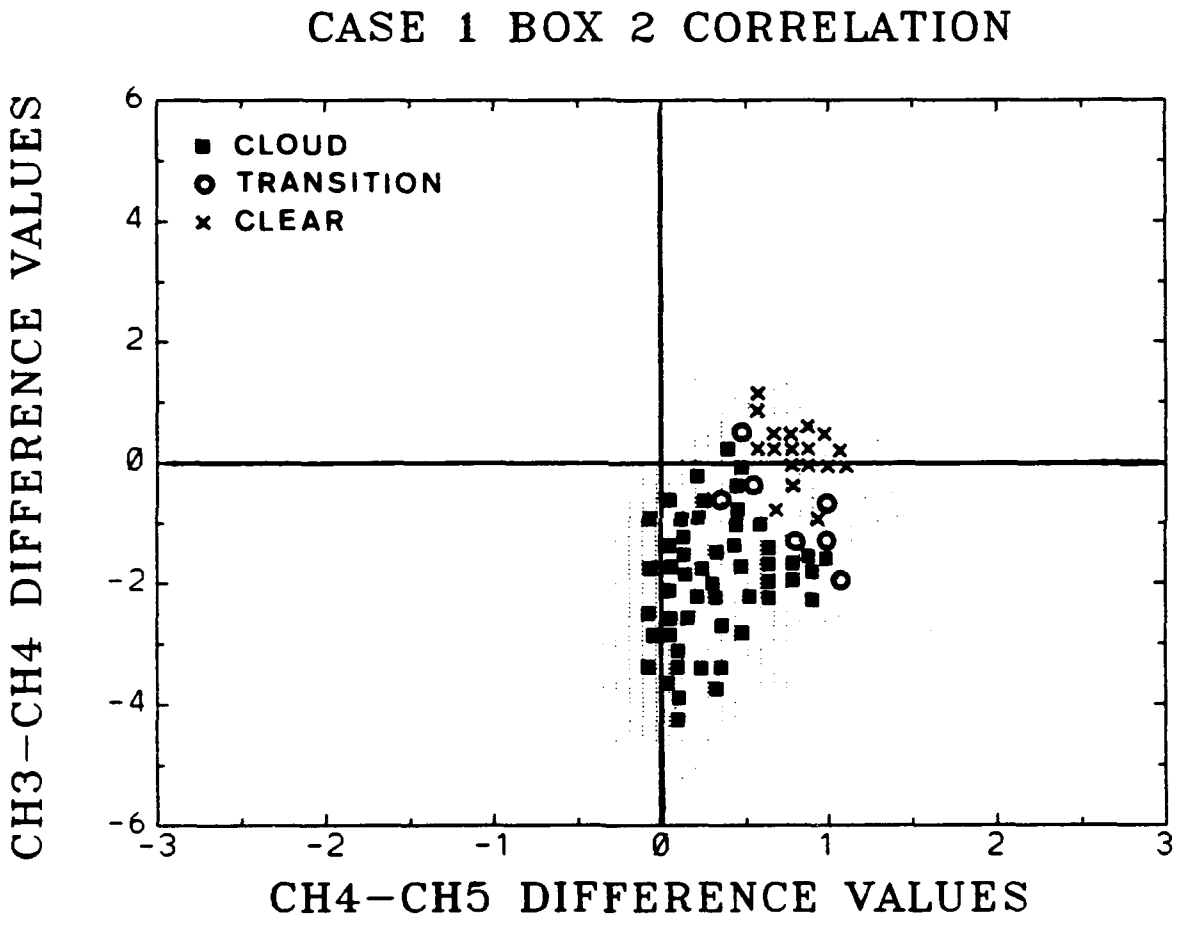

Fig. 26. Case 1, subscene 2 scatter plot reclassification.

As T_{4-5} values increased, the boundary between clear pixels and either indeterminate or cloudy ones appeared to follow a slope similar to that derived from the two subscene centroids. The intersection of the sloped threshold and a line of constant but positive T_{4-5} values could then serve as an improved threshold for both spectral difference fields between clear and cloudy pixels. At least initially, the T_{4-5} threshold was set at +.27. The sloped line shown in Fig. 24 was applied to obtain a point of intersection with the T_{4-5} line. The result was indeed a V-shaped threshold whose T_{3-4} intercept value was approximately -1.8.

In the reanalysis of subscene 2 scatter diagram (Fig. 26), the T_{4-5} boundary between clear and cloud-filled pixels was at a higher value, as expected from the higher water vapor content in the second subscene. There was still evidence of a sloped boundary as T_{4-5} values increased, but it was somewhat less pronounced than in subscene 1. Here, the T_{4-5} threshold value of +.5 was selected, and the T_{3-4} intercept of -0.8 appeared most correct.

In Fig. 27, a V-shaped threshold is applied to subscene 1 using the new threshold values obtained from the reclassified scatter diagram in Fig. 25, including the sloped threshold to account for moisture effects. Pixels found within the "V" of the threshold are colored yellow, indicating pixels deemed clear by the threshold algorithm.

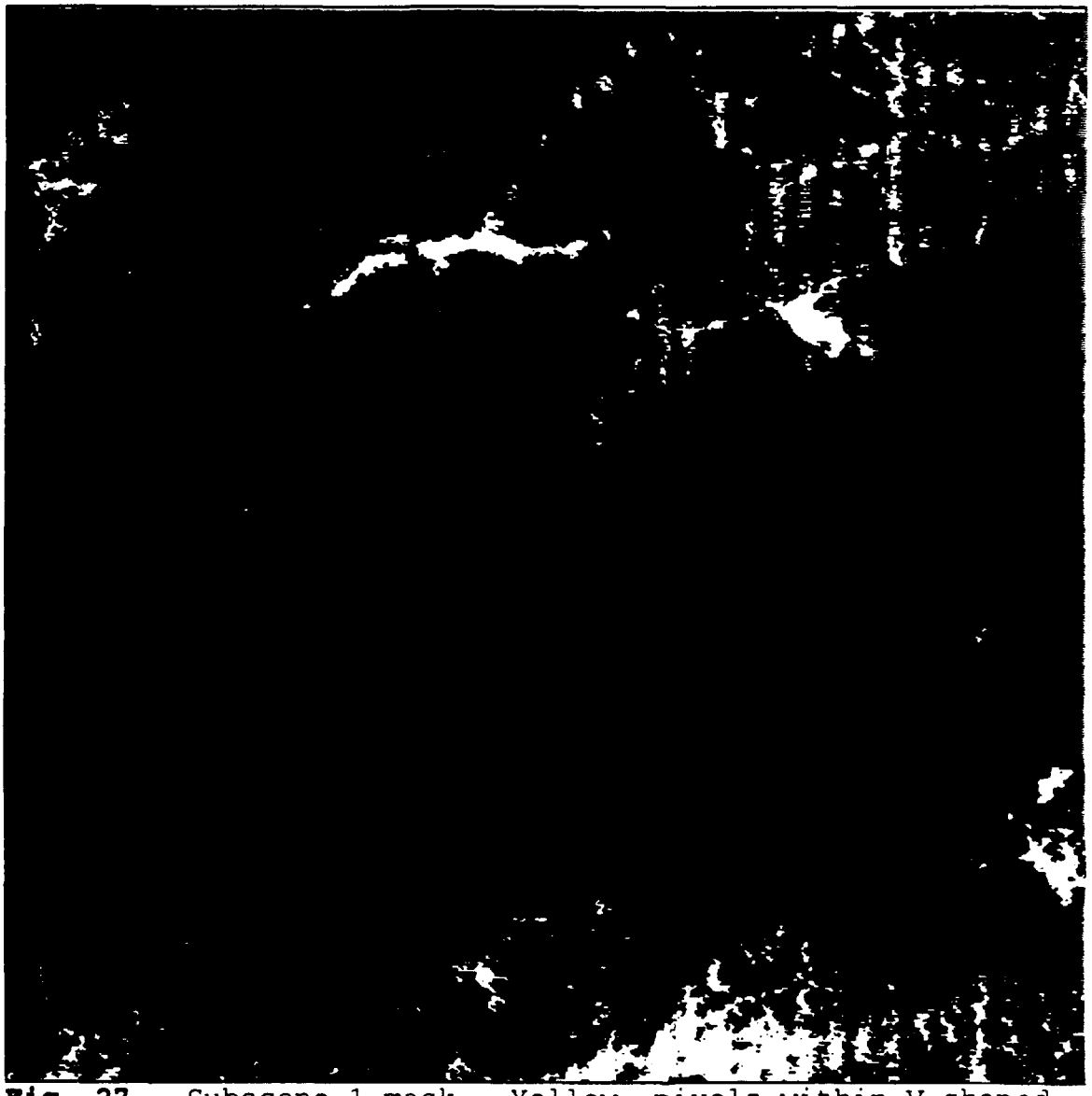

Fig. 27. Subscene 1 mask. Yellow: pixels within V-shaped threshold (T_{3-4}/T_{4-5} values of -1.8/+.27, respectively). Red: Cloudy pixels previously classified as clear.

Another mask is applied without using the sloped threshold for $H_2O_{(v)}$ correlation, and it colors those pixels red that are located below the sloped threshold but above the constant T_{3-4} line of zero slope that intersects with the constant T_{4-5} threshold.

This technique was designed to demonstrate not only an improvement in the refined threshold selection over the Dykes work, but also to show any improvement stemming directly from using the sloped threshold due to water vapor effects. Post-masking analysis confirmed that the red pixels possessed cloud contamination, and should not have been classified as clear. Yellow remained the color defining the clear regions, while red indicated the improvement in pixel classification produced by activating the sloped moisture threshold.

This double-masked image demonstrated a marked improvement over that in Fig. 23. Much of the noise signature was eliminated with the refined thresholds. Areas which previously contained ill-defined and nebulous clear regions, such as the northwest corner of the subscene, were made more distinct. Additionally, many of the red pixels not associated with noise revealed areas at cloud edges which verified as containing cloud.

The yellow and red masks were also applied to subscene 2. The results seen in Fig. 28 illustrate to a greater degree the effectiveness of the sloped threshold

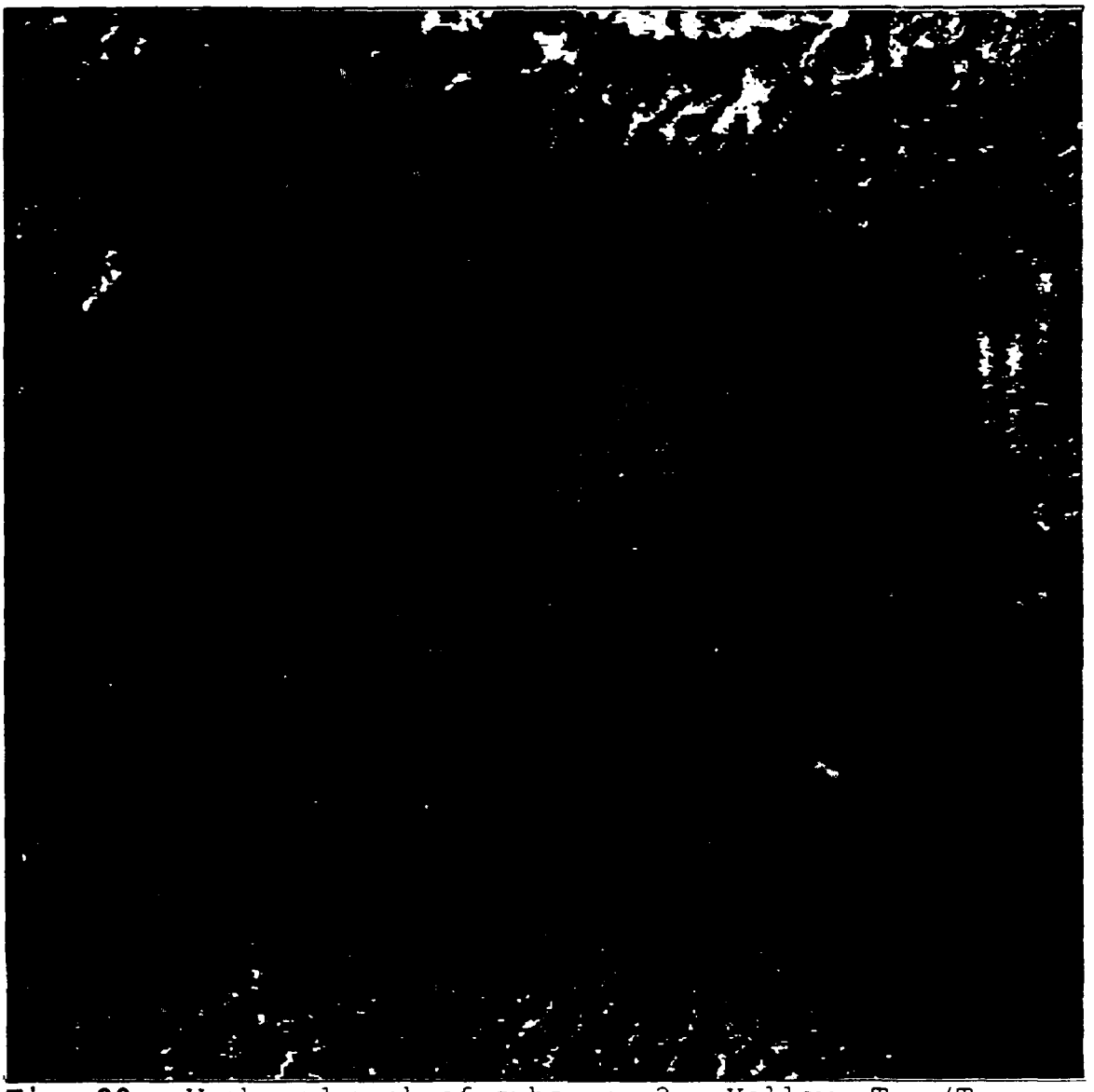

Fig. 28. V-shaped mask of subscene 2. Yellow: T_{4-5}/T_{3-4} values of +0.5/-0.8 show clear areas. Red: cloudy pixels misclassified as clear with a constant T_{3-4} value.

efforts. Most of the red pixels in this scene were found at or near breaks in the clouds, suggesting that the greatest effect of water vapor correction on cloud imaging took place at cloud edges. Cloud signatures were verified in the red pixels revealed in this image, as they were in Fig. 27. The refined masks appeared to eliminate most of the remaining noise signatures, as well.

c. Application of Thresholds to Other Subscenes

The masking thresholds in subscenes 1 and 2 showed encouraging results in identifying both apparent and "hidden" cloud in an image, and also suggested with some consistency that most misclassified pixels were located near cloud edges, especially fields of broken clouds, and in moist air. Applying the same thresholds used in subscenes 1 and 2 to other locations give encouraging results due to greater variation in cloud cover and moisture distribution. It became quickly apparent that thresholds applied to other subscenes with stronger $H_2O_{(v)}$ gradients and less cloud cover required scene-specific thresholds.

In Fig. 29, subscene 3 of case 1 displayed the identical mask used in Fig. 27 for the cloudy/dry test subscene. This mask generally established the locations of the cloud versus cloud-free air. Some areas of the subscene appear black, especially in regions at the image bottom. These are areas containing cloud but appear cloud-free in the

Fig. 29. Case 1 subscene 3 mask with V-shaped threshold. Yellow: T_{4-5}/T_{3-4} thresholds of +.27/-1.8 show clear; Red: cloudy areas once indicating clear, now suggesting cloudy

T_4 background image mask, a visual reminder of the disadvantage presented in single-channel imagery.

Figure 30 displays the corresponding color enhanced T_4 image. In this image, as shown in the T_4, T_{3-4}, and T_{4-5} overviews (Fig. 8, 10, and 12, respectively), the clear areas were generally very moist, and the cloudy areas dry. The significant water vapor gradients and apparent cloud boundaries were not present in subscenes 1 and 2.

Although some pixels possessing definite cloud signatures were still masked as clear in the northwest corner, this was an encouraging improvement over the application of the T_{3-4}-only Dykes threshold, which clearly overmasked many cloud-filled regions. The refined thresholds also eliminated most of the noise contamination present when the Dykes threshold was applied. Despite the improvement over the T_{3-4}-only threshold, the occurrance of misclassified cloudy pixels showed the T_{3-4} threshold was too low for this region.

An even greater challenge to provide credible masking thresholds was presented in subscene 1 (case 2), which contained a strong moisture gradient over a cloud/no cloud boundary, "hidden" low-level cloud near a tropical storm convective feeder band and cirrus, and a field of broken cloud with moist conditions above.

The initial masking thresholds applied were the thresholds used in the moist test case, except that the T_{4-5} threshold was modified to values between +0.5 and +1.25 to

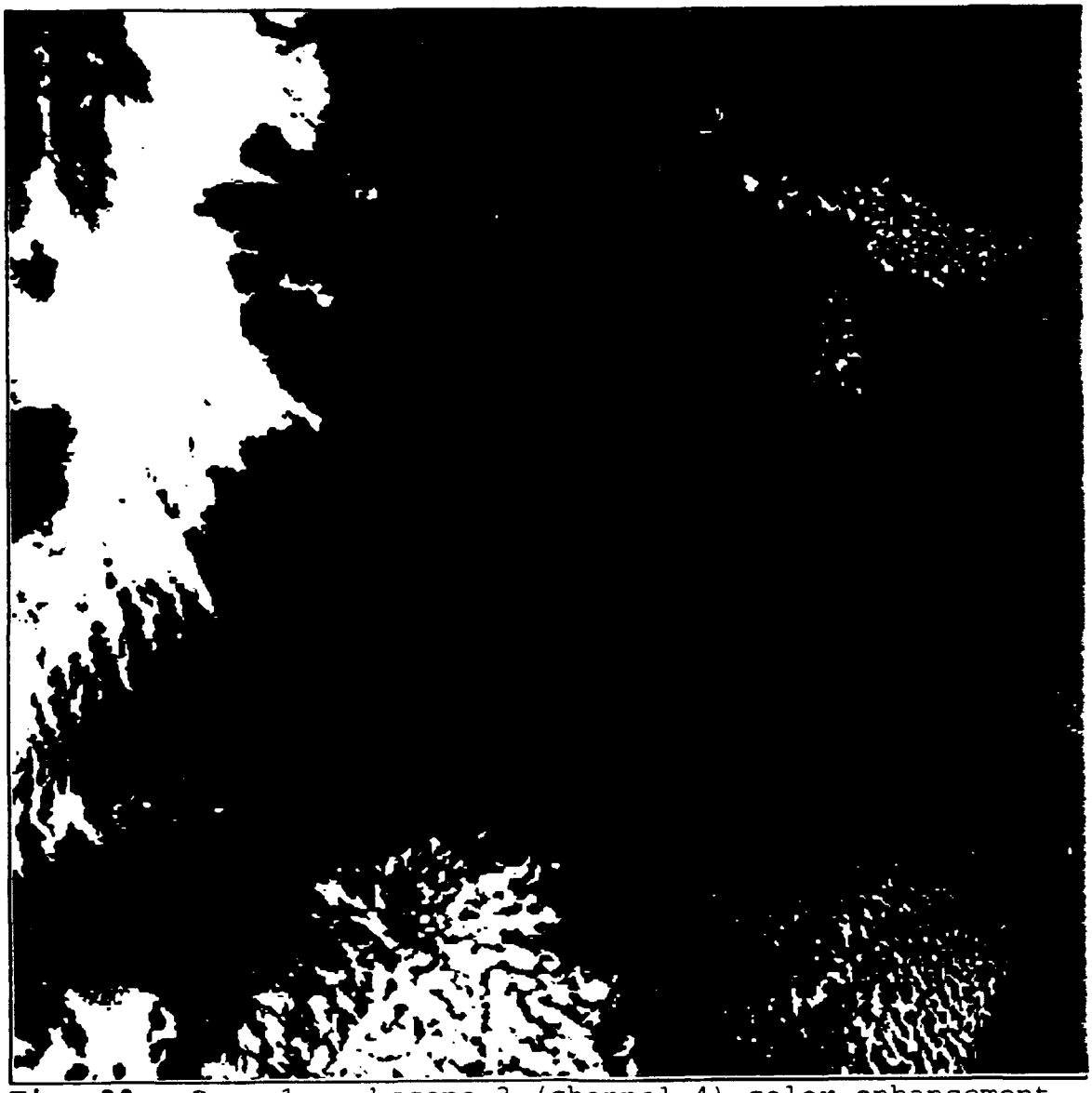

Fig. 30. Case 1, subscene 3 (channel 4) color enhancement. Yellow: cloud-free areas; red: cloudy regions.

avoid masking the cirrus, whose T_{3-4} and T_{4-5} values were high, as cloud-free. This set of thresholds was applied initially because of the significant portion of the subscene displaying relatively high T_{4-5} levels.

Figure 31 shows the results of this threshold application, and Fig. 32 displays the color enhancement. The mask in Fig. 31 showed a combination of both T_{3-4} and T_{4-5} thresholds as being too high, since much of the area north of the cirrus should have been classified as clear air with relatively high $H_2O_{(v)}$ content (see Fig. 11 and 16). The mask did identify at least some of the hidden low cloud north of the tropical storm, however. Although the color enhancement failed to reveal the hidden cloud, the yellow enhancement ably designated most clear areas and identified the fairly thin cloud over part of the Baja Peninsula in the upper right corner. Applying the threshold for the cloudy/dry test subscene colored some areas that were actually cloud, yet left some clear regions unmasked.

Additional adjustment of the T_{4-5} threshold to zero and the T_{3-4} limit to -1.25 resulted in the mask seen in Fig. 33. The hidden low cloud signature northwest of the cirrus was revealed, as was the cloudy, dry air and land over Baja. Negative T_{4-5} values prevailed in this region, and may have been caused by lower T_4 emittance from the land or cloud surface, allowing T_5 values to exceed those of T_4.

Fig. 31. Case 2, subscene 1 mask using sloped T_{4-5}/T_{3-4} thresholds of 0.5/-0.8. Yellow shows clear; red reveals yellow-masked pixels subsequently classified cloudy.

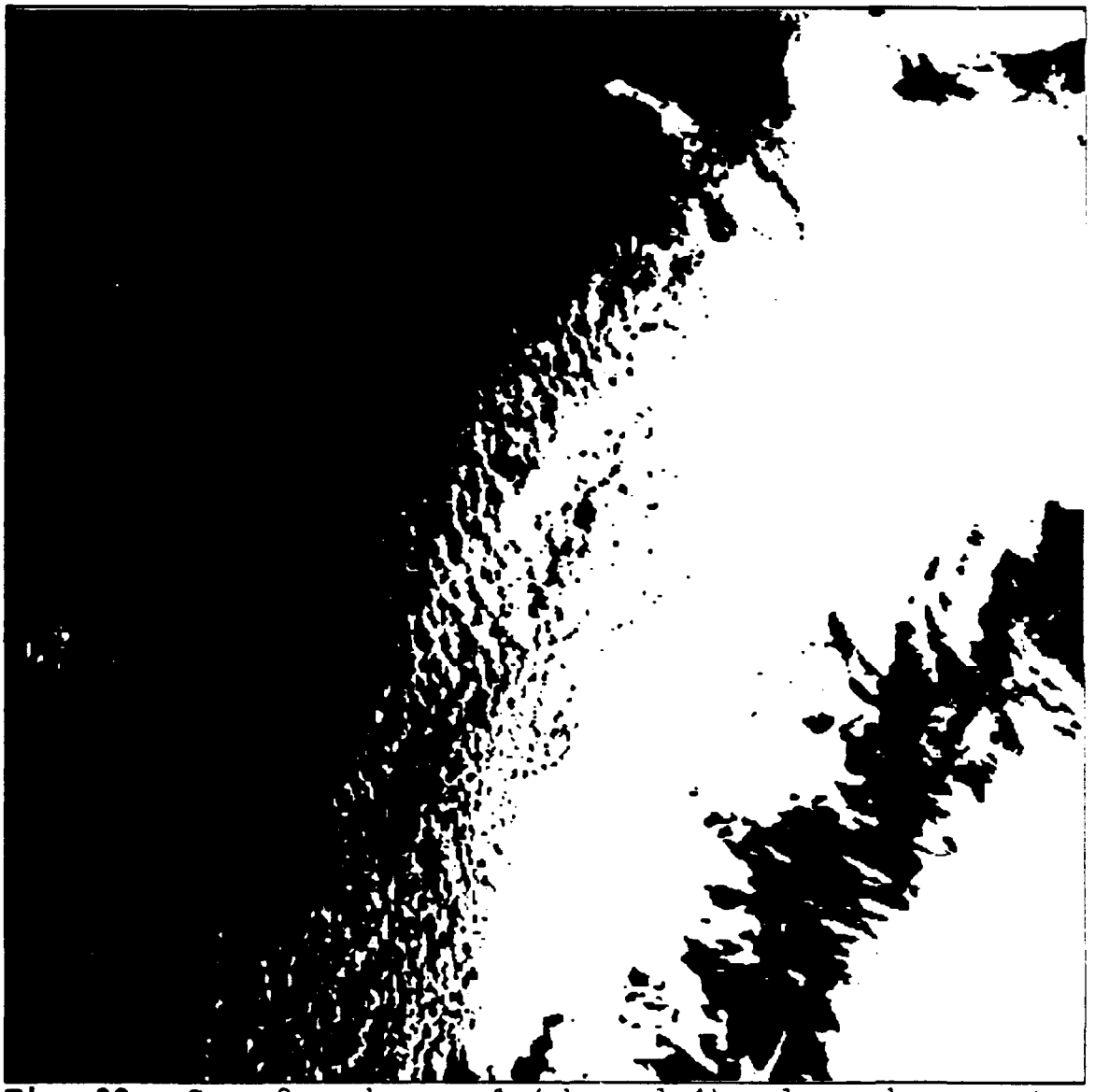

Fig. 32. Case 2, subscene 1 (channel 4) color enhancement. Yellow: cloud-free; red: cloudy.

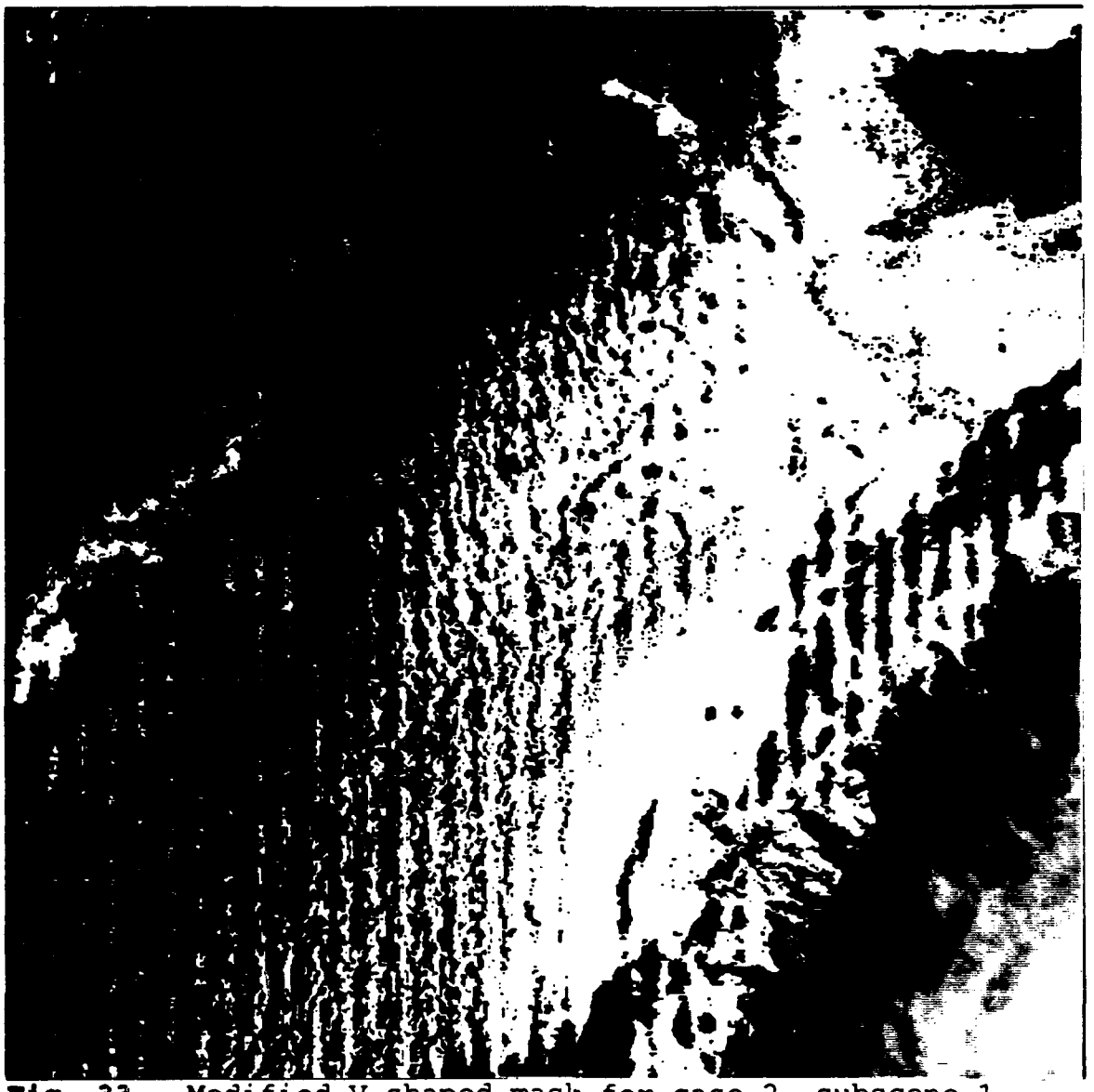

Fig. 33. Modified V-shaped mask for case 2, subscene 1. Yellow: T_{4-5}/T_{3-4} values of 0/-1.25 reveal clear. Red: improvement in cloud classification of cloudy pixels.

Finally, most of the red pixels seen in this masked image occurred at cloud boundaries in the image center where the cloud field appeared to be in transition from scattered to broken conditions and under moist air. This indicated the sloped threshold was still effectively locating misregistered clear pixels and identifying them as cloudy.

The analysis of the various subscenes in this thesis has provided the following results:

1. Successful cloud/no cloud analyses were made dependent only on the channel 3-4 differences.
2. The impact of differing amounts of water vapor on the spectral differences was evaluated.
3. Two distinct improvements to previous constant T_{3-4} thresholds were developed and tested: a sloped T_{3-4} threshold and a vertical T_{4-5} threshold.
4. These changes improved the cloud/no-cloud analyses for the cases studied even with noisy channel 3 data.

This work suggests a generalized threshold can be developed using the V-shape limits (clear pixels in the upper right quadrant). Additional study of spectral differences is needed to determine the proper shifts of the T_{4-5} threshold due to various moisture conditions.

V. CONCLUSIONS

Multispectral analysis techniques were investigated to analyze nighttime maritime clouds and water vapor patterns. Building on lessons learned in an earlier study (Dykes, 1991), spectral differencing using AVHRR T_{3-4} values produced images that revealed clouds hidden in the single-wavelength imagery which is dependent upon thermal signatures alone. Additionally, a T_{4-5} field created images illuminating the relative concentrations of water vapor in a scene. These results were supported by TOVS imagery from the HIRS channels sensitive to water vapor. Images which were created from both of these spectral difference fields accurately depicted the cloud distribution in two candidate nighttime subscenes and displayed improvement over single-channel analysis.

The correlation of low cloud and water vapor in a scene was investigated to better use spectral differences to analyze clouds. Statistical analysis revealed a positive correlation between water vapor concentration and a greater tendency for cloud to be misclassified as clear in imagery. A sloped T_{3-4} cloud/no cloud threshold was derived to account for these $H_2O_{(v)}$ effects, and constant T_{4-5} thresholds were selected. These were then applied to the candidate subscenes in the form of color masks in order to reveal cloud/no cloud boundaries

and study the classification of cloudy pixels as clear. Pixel classification improved most at cloud edges.

Selected thresholds obtained from analysis of two candidate subscenes were applied to other scenes of varying $H_2O_{(v)}$ concentration with some success. Results indicated that threshold value selection needed to be completed on a by-case basis, although the slope derived in the test cases continued to identify in a suitable way the pixels requiring reclassification. Most pixel classification continued to occur in areas containing high $H_2O_{(v)}$ values over fields of broken clouds. Presence of noise in channel 3 (and therefore the T_{3-4}) products made the analysis of these cases more difficult.

Future study should establish a way to quantify shifts in T_{4-5} thresholds to account for water vapor variations. This would generalize the application of thresholds for image classification and would permit improved representation of clouds in image subscenes possessing a broad spectrum of cloud and water vapor features.

LIST OF REFERENCES

Crosiar, C., T.F. Lee, and A. Caughey, 1989: Nighttime cloud classification using two infrared channels of the AVHRR. *Preprints of Twelfth Meteorological Conference in Weather Analysis and Forecasting*, Amer. Meteor. Soc., Boston, MA, 330-333.

d'Entremont, R. P., 1986: Low- and midlevel cloud analysis using nighttime multispectral imagery. *Journ. Climate and Applied Met.*, **25**, 1853-1869.

Dykes, J. D., 1991: Multispectral analysis of nighttime low clouds over the ocean. M.S. Thesis, Naval Postgraduate School, Monterey, CA, 42pp.

Eyre, J.R., J.L. Brownscombe, and R.J. Allam, 1984: Detection of fog at night using advanced very high resolution radiometer imagery. *Meteorological Magazine*, **113**, 266-271.

Goody, R. M. and Y. L. Yung, 1989: *Atmospheric Radiation: Theoretical Basis,* 2nd ed. Oxford Univ. Press, Oxford and New York.

Hunt, G.E., 1973: Radiative properties of terrestrial clouds at visible and infrared thermal window wavelengths. *Quart. Journ. Royal Meteor. Soc.*, **99**, 346-359.

Olesen, F.S. and H. Grassl, 1984: Cloud detection and classification over oceans at night with NOAA-7. *Int. Journ. Remote Sensing*, **6**, 1435-1444.

Saunders, R.W. and K.T. Kriebel, 1988: An improved method for detecting clear sky and cloudy radiances from AVHRR data. *Int. Journ. Remote Sensing*, **9**, 123-150.

Smith, W.L., H. M. Woolf, C. M. Hayden, D. Q. Wark, and L. M. McMillin, 1979: The TIROS-N operational vertical sounder. *Bull. Amer. Meteor. Soc., 60,* 1177.

Valley, S.L. (ed.), 1965. *Handbook of Geophysics and Space Environments.* Air Force Cambridge Research Laboratory, Hanscom AFB, MA.

INITIAL DISTRIBUTION LIST

1	Defense Technical Information Center Cameron Station Alexandria, VA 22304-6145	2
2.	Library, Code 0142 Naval Postgraduate School Monterey, CA 93943-5002	2
3.	Chairman (Code MR) Department of Meteorology Naval Postgraduate School Monterey, CA 93943-5000	1
4.	Professor Philip A. Durkee (Code MR/DE) Department of Meteorology Naval Postgraduate School Monterey, CA 93943-5000	2
5.	Professor Carlyle H. Wash (Code MR/WX) Department of Meteorology Naval Postgraduate School Monterey, CA 93943-5000	2
6.	Captain Christopher K. Brooks NOCC/JTWC PSC 489 Box 17 FPO AP 96540-0051	2
7.	Commander Air Weather Service Scott Air Force Base, IL 62225-5008	1
8.	Commander Air Force Global Weather Central Offutt Air Force Base, NE 68113	1
9.	USAF ETAC/LD Air Weather Service Technical Library Scott Air Force Base, IL 62225-5008	1
10.	Program Manager AFIT/CI Wright-Patterson Air Force Base, OH 45433-6853	1